*Dissertation*

# Data-driven construction of holographic QCD model

Takayuki Sumimoto

January 31, 2023

*Department of Physics, Osaka university*

**Abstract**

The gauge/gravity correspondence is the duality between gauge theories and field theories on curved spacetime in one higher dimension. It has been studied as a crucial key to defining a quantum gravity. Despite its importance, a way to find a gravitational system dual to a given quantum field theory is not well understood. Particularly important quantum field theories are those with Yang-Mills sectors, including QCD, whose large $N_c$ and strong coupling limit are believed to give a classical gravity dual. This class of gravity dual is called "holographic QCD". Although we are still lacking in how to construct the dual beyond the large $N_c$ limit, inspired by such a class of correspondences, methodologies to describe QCD phenomena with field theories on curved background have been explored. Among them, the AdS/QCD models are field theories on asymptotic AdS spacetime which breaks conformal symmetry to describe the low energy physics of QCD. As a further development of the methodologies, improved holographic QCD is based on the five-dimensional Einstein-dilaton system with a non-trivial dilaton potential. Once a model of IHQCD is completely determined, we expect to learn fruitful lessons for how we can construct a gravity dual to a given quantum field theory, in which a clue of a quantum gravity is hidden. So phenomenological approach is an interesting and important direction for studying holographic QCD.

Since a holographic QCD model should be consistent with QCD, the construction of the model can be regarded as derivation of the appropriate model from experimental data. Previous works construct simple models with a few parameters, which are fixed from as many values as the parameters from the experimental data, but simple models are limited to show the agreement with the data far from the inputs. So, it is important to establish the way constructing a more complicated model.

To tackle such problem, we explore the data-driven framework to construct holographic QCD models. Our strategy consists of two steps in the construction.

The first step is the derivation of an AdS/QCD model, where bulk gravitational fields are treated as background ones. We proposed a deep learning method to build an AdS/QCD model from the data of hadron spectra. A large ambiguity is allowed for the bulk gravitational field with which QCD observables are holographically calculated. I adopt the experimentally measured spectra of $\rho$ and $a_2$ mesons as training data and perform supervised machine learning which determines concretely a metric and a dilaton field in the setup of the AdS/QCD model. The deep learning architecture is based on the

AdS/DL correspondence where the deep neural network is identified with the emergent bulk spacetime.

The second step is derivation of an explicit form of the dilaton potential in improved holographic QCD from the above background fields obtained in the first step. We conduct the derivation with the $\rho$ meson spectrum case and chiral condensate case, respectively. The former case is associated with a zero-temperature metric, and the latter data comes from the lattice calculation. Requiring that the gravitational fields are a solution to the Einstein-dilaton action derives the corresponding dilaton potential backward.

These derivations are the first example of the data-driven construction of IHQCD. In addition, these procedure enables us to obtain the metric and dilaton fields as the solutions to the Einstein equation. This ensures that the deep learning proposal is a consistent gravity. Furthermore, we find that the resulting dilaton potential satisfies the requirements normally imposed for IHQCD, and that the holographic Wilson loop for the derived model exhibits quark confinement at zero temperature. We show the usefulness of the model with the prediction at finite temperature that the string breaking distance is found to be consistent with another lattice QCD data.

# Acknowledgments

I would like to express my great appreciation to many people for kind support and help. First and foremost, I would like to thank Prof. Koji Hashimoto for having supervised me during three years until the first year of my doctoral course in addition to keeping discussion and education after moving to Kyoto university. I owe deep gratitude to my collaborators Tetsuya Akutagawa and Keisuke Ohashi. I have been enjoying discussion of physics with them and this thesis is based on the collaboration with them. I would like to sincerely appreciate to Prof. Tetsuya Onogi and Prof. Tatsuma Nishioka for being my supervisor in the second and the last year of my doctoral course. They have given to me much of advice not only on my research but also on my career. Prof. Tatsuma Nishioka also have kindly helped me for improving my presentation and the manuscript of this thesis. I am also grateful to Prof. Shinya Kanemura, Prof. Atushi Hosaka and Prof. Hidenori Fukaya for reading the manuscript of this thesis carefully and giving me useful comments.

I would like to thank to Mika Umetani, Satomi Suzuki, Kazumi Asano and Akiko Takao, the secretaries of particle physics theory group at Osaka university for supporting a lot in my student life. I am also grateful to all members of my laboratory for making my experience in this group quite fruitful and enjoyable. During my doctoral course, I have been supported by JSPS fellowship for Young Scientists. Finally, I wish to thank my parents for their understanding, love and constant support throughout my life at Osaka university.

# Contents

# 1 Introduction

Over the past decades, gauge/gravity duality has been one of the most important subjects in theoretical physics. The duality gave the novel perspective to the study of quantum gravity and strongly coupled system. The most influential study of the gauge/gravity duality is referred to as AdS/CFT correspondence [1]. The fact that the D-brane can be described theoretically from two different perspectives is at the heart of the AdS/CFT correspondence conjectured in 1997 [1], by Maldacena. This conjecture provides a mapping between supersymmetric, strongly coupled large $N_c$ gauge theories and weakly coupled supergravity theories in one higher dimensional spacetime. This gauge theory is just the simplest 3+1 -dimensional theory that appears on the world volume of the most basic D3 brane configuration; given $N_c$ D3 branes coinciding in a certain location, one can realize a $SU(N_c)$ gauge theory in the low energy limit. The quantum field theory is an $\mathcal{N} = 4$ large $N_c$ $SU(N_c)$ gauge theory. The $\beta$ functions have been shown to vanish to all orders in perturbation theory and are conformal even after quantization. $N_c$ must be large because a very large number of D3 branes is needed to ensure that the supergravity approximate the string theory safely. Many nontrivial tests have been found for this original case and the correspondence conjectured with other D-branes, and no evidence to deny the conjecture have been reported.

Particularly important quantum field theories are those with Yang-Mills sectors, including QCD, whose large $N_c$ and strong coupling limit are believed to give a classical gravity dual. This class of gravity dual is called “holographic QCD”. Although we are still lacking in how to construct the dual beyond the limit, inspired by such class of correspondence, methodologies to describe QCD phenomena with field theories on curved background have been explored. Among them, the AdS/QCD models are field theories on phenomenological modifications of the AdS spacetime making conformal symmetry of the bulk broken to describe the physics of hadrons and QCD. As a further development of the methodologies, improved holographic QCD is based on the five dimensional Einstein-dilaton system with a non-trivial dilaton potential. Once a model of IHQCD is completely determined, it is believed to learn fruitful lessons related to how we can construct a gravity dual to a given quantum field theory, in which a clue of a quantum gravity is hidden. So phenomenological approach, also called bottom-up approach, is an interesting and important direction in which one studies holographic QCD.

The string theory “top-down” construction does not solve the problem, because it merely provides examples as a pair of a gravity and a QFT at the same time. Many excellent works provided a pair in which the QFT side resembles a given target QFT.

A lot of effort has been put to seek for a gravity dual of QCD, as QCD is the renowned, and realistic QFT among all.

It should be emphasized that once a classical gravity system is given, the dual QFT quantities can be easily calculated by the AdS/CFT dictionary. The problem is how we can go backwards: for a given QFT correlators, how we can get the gravity system. To solve this kind of inverse problems, we need special techniques. A strongly coupled QFT consists of a vast amount of data, such as $n$-point correlators for infinite kinds of local/non-local gauge invariant operators. Furthermore, QCD is a part of the Standard Model for which a lot of experimental data is available. To this end, machine learning method may help us. If there exists a gravity dual of QCD which is simple enough with a finite number of parameters, the features of the data of QCD needs to be efficiently extracted, by solving the AdS/CFT backwards. Deep learning [2, 3, 4] which technically advanced these years may shed light on the fatal problem of the AdS/CFT.

In Ref. [5], deep learning was applied to determine an emergent gravity metric from a given data of a QFT. The dictionary used was for a one-point function of an operator in the QFT, corresponding to a bulk field value in the dual gravity system. In Ref. [6], the method was applied to lattice QCD data of a chiral condensate, to find a metric of the gravity system dual to QCD. Based on the success of this method working for one-point functions, in this paper we make one more step toward realistic QCD. We use hadronic two-point functions, *i.e.* the hadron spectra which are measured in experiments.

The most well-observed quantities in experiments for QCD are hadron spectra and hadron couplings. The best framework to test the deep learning method is the AdS/QCD [7, 8, 9], a bottom-up construction of phenomenological gravity models based on symmetries and the dictionary. It is known that the simple AdS/QCD framework can host lots of QCD quantities including hadron spectra. Here, again, the conventional methods in the AdS/QCD are first to come up with a gravity model to calculate the QCD quantities from the model and then to compare those with experimental data. If the quantity does not match well, one throws away the gravity model and try again with a different gravity model. The gravity model has a large arbitrariness, and in addition the dictionary is non-local, so solving the inverse problem is challenging. This is the reason why the deep learning method can help finding the gravity dual of QCD.

The AdS/DL correspondence in Ref. [5] was invented due to the similarity between the deep neural network (DNN) and bulk gravity system.[1] In the training, weights of the neural network are trained and determined by machine, which is regarded as

[1]For a detailed relation, see Ref. [10]. An early study on the similarity between the AdS/CFT and the DL is in Ref. [11]. See Refs. [12, 13] for related essays. A continuum limit of the deep layers was studied in a different context [14].

an emergence of the spacetime, as the differential equation on the discretized gravity spacetime is regarded as a propagation of information on the deep neural network, with the depth direction identified with the AdS radial direction.

The goal of this paper is to construct a gravity model from spectral data, and specifically, with the soft wall model in mind, we aim to identify the background field $B(z)$ of the model as unknown by deep learning.

The organization of this dissertation is as follows. We begin in section 2 with a brief description of basic facts and previous research, including a short summary of gauge/gravity duality, example of holographic QCD models and idea of deep learning application to the holographic modeling. In section 3 we describe the concrete example of construction of a holographic model in the way of deep learning. We consider the vector meson sector along with the soft wall model [9] and the five-dimensional geometry is constructed with mass spectrum of low-level excitation of $\rho$ meson. This section is based on our publication [15]. We show the first attempt to get the properties of the metric and the dilaton field by considering the higher spin meson sector construction with mass spectrum of $a_2$ meson and some comments for the subtle point about this attempt in section 3.2. In section 4 we consider the Einstein-dilaton system with an undetermined dilaton potential, which is derived from the geometry constructed in the previous section. This derivation includes the process to solve Einstein equations for the metric and the dilaton field. The calculation of holographic Wilson loop with the resultant metric describes quark confinement as the linear behavior of the quark-antiquark potential. This section is based on our publication [16]. In section 5 we derive the dilaton potential from the lattice data of the chiral condensate as a function of the quark mass. Contrast to the previous section, the black hole ansatz for the metric is employed reflecting that the lattice data is the observables in the non-zero temperature. Our model describes the confinement again and the predicted QCD-string breaking distance shows the good agreement with the lattice calculation. This section is based on our publication [17]. We conclude the thesis with some future direction in section 6.

# 2 Basics

## 2.1 Basics of gauge/gravity duality

The gauge/gravity duality comes from the open/closed string perspective of the string theory on $N$ D-branes. Open string perspective reduces to the Yang-Mills theory with superconformal symmetry, in which the coupling $g_{YM}$ is a parameter, while closed string perspective yields the string theory on $\mathrm{AdS}_5 \times S^5$, in which the string coupling $g_s$, squared string length $\alpha'$ and AdS radius $L$ are parameters. The duality between these two effective theories leads the AdS/CFT dictionary;

$$g_{YM}^2 = 2\pi g_s, \qquad g_{YM}^2 N = L^4/\alpha'^2. \tag{2.1}$$

Since the two theories are equivalent, it is expected that there is a relation between the physical quantities as well the AdS/CFT dictionary (2.1). Of particular importance in the gauge-gravity correspondence is the one-to-one correspondence, called the field/operator correspondence, between the field on the gravity theory side and the (gauge-invariant) operator on the gauge theory side. The relation for the generating functionals that follows from the field/operator correspondence is called the GKP-Witten relation, which provides a prescription for obtaining the correlation functions of the gauge theory in the gravity theory side calculation [18, 19].

It is important to note that the AdS spacetime is bounded. The field/operator correspondence is derived from the behavior of the fields near the boundary. The gravity theory side is often referred to as "bulk" because it is surrounded by such a boundary. The field on the gravity theory side is accordingly called the bulk field.

To show the concrete form of the field/operator correspondence, we use a simple example of a $d+1$-dimensional scalar field and discuss how the scalar operator of the corresponding $d$-dimensional theory appears in concrete form. In addition, we will discuss the relation between the generating functionals of gauge and gravity theories derived from the correspondence.

The action for bulk scalar field on $\mathrm{AdS}_{d+1}$ spacetime up to quadratic term is

$$S = \frac{C}{2}\int d^{d+1}x\sqrt{-g}\left(-\frac{1}{2}(\partial\phi)^2 - \frac{1}{2}m^2\phi^2\right). \tag{2.2}$$

Introducing Poincaré coordinate metric for $\mathrm{AdS}_{d+1}$ spacetime

$$ds^2 = \frac{L^2}{z^2}\left(dz^2 + \eta_{\mu\nu}dx^\mu dx^\nu\right) \qquad (z > 0), \tag{2.3}$$

the equation of motion for scalar field is

$$-\frac{1}{\sqrt{-g}}\partial_\mu\sqrt{-g}g^{\mu\nu}\partial_\nu\phi(x,z)+m^2\phi(x,z)=0. \tag{2.4}$$

To see asymptotic behavior of $\phi$ near the boundary, let us take $\phi$ as a polynomial $\phi = z^\lambda$ and compute $\lambda$ for $z \sim 0$.

$$\left(-z^{d+1}\partial_z z^{-(d+1)}z^2\partial_z+m^2\right)z^\lambda=0 \tag{2.5}$$

$$\left(-\frac{\lambda(\lambda-d)}{L^2}+m^2\right)z^\lambda=0. \tag{2.6}$$

One can say $\lambda$ is either one of the solutions of this differential equation $\Delta_\pm$,

$$\Delta_\pm=\frac{d}{2}\pm\sqrt{\left(\frac{d}{2}\right)^2+m^2L^2}. \tag{2.7}$$

Therefore, the asymptotic solution for the equation of motion (2.4) can be written as

$$\phi(z\to 0,x)\sim\alpha(x)z^{\Delta_-}+\beta(x)z^{\Delta_+}+\cdots. \tag{2.8}$$

The first term is the non-normalizable mode making the action (2.2) diverse, while the second term is normalizable mode. non-normalizable mode $\alpha(x)$ defines the boundary condition on $z = 0$ as

$$\alpha(x)=\lim_{z\to 0}\phi(x,z)z^{-\Delta_-}. \tag{2.9}$$

Since $\phi$ is a scalar, conformal dimension is 0. By dimensional analysis, $\alpha$ and $\beta$ has conformal dimension $\Delta_-$, $\Delta_+$ respectively.

We see the example for scalar bulk field, more generally, there are relationships for vector or other representation. When we have bulk $p$-form field, the generalized formula is

$$(\Delta-p)(\Delta-p-d)=m^2L^2. \tag{2.10}$$

This equation gives us the relationship between the dimension of the operator and the mass of the bulk field, so that when we have an operator to consider on the gauge theory side, we can immediately determine the mass of the bulk field.

The equivalence between gravity theory and gauge theory can also be said to be the coincidence of their partition functions. We saw that the bulk normalizable modes correspond to the source on the gauge theory side above but let us consider the partition function when the source is included in the gauge theory.

Supposed that we have a gauge invariant operator $O_\Delta(x)$ introduced by source $J(x)$. The whole action of gouge theory side is $S_{\text{gauge}} - \int d^d x J(x) O_\Delta(x)$ then its partition function is

$$Z[J(x,t)] = e^{-W[J(x)]} = \left\langle \int d^d x J(x) O_\Delta(x) \right\rangle_{gauge} \tag{2.11}$$

where $W[J]$ is a generating functional.

On the other hand, the saddle point approximation is valid in gravity theory side when the large $N$ and $\lambda$ limit is taken,

$$Z_{\text{gravity}} = \exp\left(S_{\text{gravity}}[\phi]\right). \tag{2.12}$$

Therefore, the generating function in (2.11) can be identified to on-shell action of $S_{\text{gravity}}$. $\phi$ denotes the bulk field then the boundary condition (2.9) should be imposed. Finally, we get the following formula for the generating functional is following.

$$W[J(x)] = S_{\text{gravity}}\Big|_{\lim_{z\to 0}\left(\phi(x,z)z^{\delta-d}\right)=J(x)}. \tag{2.13}$$

In this way, we have obtained the formula to evaluate the correlation functions of a gauge theory by a classical gravity theory. It should be noted that the large $\lambda$ limit is taken. In other words, the GKP-Witten formula provides a method to calculate the correlation functions of strongly coupled gauge theories to which perturbation calculations cannot be applied.

## 2.2 Basics of AdS/QCD

In the previous section, we saw that the GKP-Witten relation can be used to obtain the correlation function of the CFT by replacing it with the gravity theory side of the calculation. Thus, the gauge-gravity correspondence is one tool to study strongly coupled gauge theories. Therefore, it is a natural attempt to replace the strongly coupled gauge theory, QCD, with the calculation of gravity theory. Such an attempt is called holographic QCD.

However, the problem in discussing the duality of QCD based on the D-brane consideration as discussed in section 2.1 is that the gauge theory has large $N_c$ color degrees of freedom instead of $N_c = 3$.

Nevertheless, it can also describe dynamics characteristic of QCD and other noncommutative gauge theories, such as chiral symmetry and confinement properties. For example, the addition of $N_f$ D-branes as probes can introduce flavors into Large $N_c$

gauge theories to describe quarks in their fundamental representation [20, 21]. The mesons treated in this context show similar behavior to QCD [22, 23].

On the other hand, there are approaches that are not based on the low-energy picture of D-branes but use a phenomenologically determined five-dimensional gravity model based on the assumption that a dual gravity theory exists for QCD. Among which, the AdS/QCD model [7, 8, 9] is to provide a simple phenomenological model in 5-dimensional curved spacetime which describes desired sectors of QCD effectively. The 5-dimensional Lagrangian is built under the guide of the AdS/CFT dictionary. For example, to compute hadron mass spectra, one introduces fields propagating in a 5-dimensional curved spacetime which are dual to the hadrons of concern. One of the most popular models of AdS/QCD is so-called soft-wall models given in Ref. [9] where, rather than using a brute cut-off of the 5-dimensional geometry as in the inaugural work [7, 8], one introduces a 5-dimensional dilaton field to realize a smooth wall to confine fields in the curved geometry, which enables discussions on a part of the QCD Regge trajectories.

For a five-dimensional model, consider an effective theory that includes a field corresponding to the physical quantity you wish to consider on the QCD side. If the operator is known, the field to be included in five-dimensional model can be determined from the field/operator correspondence. In the case of chiral dynamics with quarks, we can consider a theory that includes chiral condensation, a scalar field corresponding to chiral current, and a gauge field. The masses of the fields are determined from the (2.10) as follows, respectively.

$$\text{Chiral condensation } \bar{q}q \quad : \quad m^2 = \Delta(\Delta - 4) = -3, \tag{2.14}$$

$$\text{current } \bar{q}\gamma^\mu q \quad : \quad m^2 = (\Delta - 1)(\Delta - 3) = 0. \tag{2.15}$$

The symmetry from flavor $SU(N_f)_L, SU(N_f)_R$ is realize as the local symmetry.

In AdS/QCD, gravity is more concerned with whether the model yields result consistent with QCD than whether it is a solution to a supergravity theory. In this sense, it is a bottom-up approach. As a way of taking the space-time of the bulk, for example

- Hard wall model [7]
  A cutoff is considered in the dynamic radial direction with respect to $AdS_5$ space-time.

- Soft wall model [9]
  A model that considers $AdS_5$ space-time plus non-trivial dilaton.

The hard wall model was the first AdS/QCD model. Soon after, the soft wall model was proposed to reproduce the spectra of mesons that could not be reproduced by the hard wall model.

In this section, we will review the method for calculating the spectrum of a meson using these two models as examples. From now on, the Greek letters $\mu, \nu, \cdots = 0, 1, 2, 3$ as the subscripts of Lorentz will represent the directions of 4-dimensional space-time on the field theory side, and the capital alphabet $M, N, \cdots = 0, 1, 2, 3, 4$ represent the directions of five-dimensional space-time in bulk theory. If we focus only on the direction, $V_4$ may be denoted by $V_z$, etc. In this chapter, for simplicity, we will take units such that the AdS radius $L$ is 1.

Generically, any AdS/QCD model is given in the following manner. First, one assumes the existence of an effective theory which is holographically dual to QCD via the AdS/CFT correspondence. Next, based on the well-known dictionary of the AdS/CFT, one writes the 5-dimensional bulk action of the theory, with ingredients necessary to reproduce a QCD sector of one's concern. For example, for flavor symmetry, one introduces corresponding gauge symmetry in the bulk theory. The associated gauge bosons in 5 dimensions correspond to the flavor current operators in QCD, which are nothing but the vector mesons. The gauge bosons are in a 5-dimensional curved spacetime whose gravity metric and bulk dilaton field are prearranged.

### 2.2.1 Hard wall model

The hard wall model is a model that introduces a cutoff in five-dimensional AdS spacetime.

$$ds^2 = \frac{1}{z^2}\left(dz^2 + \eta_{\mu\nu}dx^\mu dx^\nu\right), \qquad 0 < z \leq z_0 \tag{2.16}$$

The cutoff $Z_0$ breaks the scale invariance of the AdS spacetime. It is known that such a spacetime with a cutoff also appears in the low-energy picture of D-branes. The scale of the cutoff is considered to correspond to the mass gap due to confinement on the gauge theory side, and it is natural to consider such a spacetime as an AdS/QCD model.

As a theory on such a background spacetime, let us consider an effective theory describing the dynamics of pseudo scalar, vector, and axial vector mesons.

The pseudo scalar, pion, appears as Nambu-Goldstone bosons when the chiral symmetry is spontaneously broken by the vacuum expectation value of the chiral condensate. The bulk field corresponding to the chiral condensation is a scalar field with mass $m^2 = -3$, as we saw in (2.14). Let $X(z, x)$ denote this. Following the treatment of chiral perturbation theory, let this $X(z,x)$ be

$$X(z,x) = X_0(z) e^{2i\pi(x)}. \tag{2.17}$$

The field $\pi^a(x)$ corresponding to the pion appears when the resulting chiral symmetry is broken. In fact, the $X_0(z)$ part of the asymptotic behavior is the same for the chiral condensate $\Sigma$ and its source, the quark mass $M$

$$X_0 \sim Mz + \Sigma z^3 \tag{2.18}$$

is expected from (2.8).

As vectors and axial vectors, we introduce dual massless vector fields in the chiral symmetry currents $\bar{\psi}_L \gamma \psi_L$, $\bar{\psi}_R \gamma \psi_R$.

Summing up the above, the effective action we wish to consider can be written as follows.

$$I = -\int d^4x \int_0^{z_0} dz \sqrt{-g}\, \mathrm{Tr}\left[ |DX| + 3|X|^2 + \frac{1}{4g_5^2}\left(F_L^2 + F_R^2\right)\right] \tag{2.19}$$

Let $X$ be a matrix and transform as a bifundamental representation of $U(1)_L \times U(1)_R$ gauge symmetry.

$$D_\mu X = \partial_\mu X - iA_\mu^L X - iXA_\mu^R \tag{2.20}$$

In the boundary condition (2.18) for $X$, diagonalizing for simplicity $M = m_q \mathbb{1}$,$\sigma = \sigma \mathbb{1}$, there are four parameters for this model: $m_q, \sigma, z_0, g_5$. It has been reported that by tuning these four parameters, the [7] was able to predict the seven physical quantities shown in Table 2.1 with an error of about 10%.

| Observables | Experimental Observed (MeV) | Predicted (MeV) |
|---|---|---|
| $m_\pi$ | 139.6 ± 0.0004 | 141 |
| $m_\rho$ | 775.8 ± 0.5 | 832 |
| $m_{a_1}$ | 1230 ± 40 | 1220 |
| $f_\pi$ | 92.4 ± 0.35 | 84.0 |
| $F_\rho^{\frac{1}{2}}$ | 345 ± 8 | 353 |
| $F_{a_1}^{\frac{1}{2}}$ | 433 ± 13 | 440 |
| $g_{\rho\pi\pi}$ | 6.03 ± 0.07 | 5.29 |

Table 2.1: Comparison of the physical quantities of the meson fitted by the hard wall model with its experimental observations. All values are taken from [7].

Among these predictions, we will make calculations especially for the spectra of $\rho$ mesons, which are vector mesons.

(2.19) of vector sector

$$V^M = \frac{A_R^M + A_L^M}{2}. \tag{2.21}$$

We shall express this in the following way. The leading contribution of the spectrum can be calculated from the kinetic terms of this $V$.

$$I_{\text{vector}} = -\frac{1}{4g_5^2}\int_0^{z_0} dz d^4x \sqrt{-g}\big(\partial_{[M} V_{N]}\big)^2 \tag{2.22}$$

where only one flavor is considered here using flavor symmetry for simplicity.

The condition for fixing gauge

$$V^z = 0, \qquad \partial_\mu V^\mu = 0 \tag{2.23}$$

is imposed then

$$I_{\text{vector}} = -\frac{1}{4g_5^2}\int_0^{z_0} dz d^4x \sqrt{-g} g^{zz}\eta^{\mu\nu}\big(\partial_z V_\mu \partial_z V_\nu + 2V_\mu \partial^2 V_\nu\big), \tag{2.24}$$

$$= -\frac{1}{4g_5^2}\int_0^{z_0} dz d^4x \frac{1}{z}\Big(\partial_z V_\mu \partial_z V^\mu + 2V_\mu \partial^2 V^\mu\Big). \tag{2.25}$$

Now we want to find the equation of motion in $z$ direction, but for simplicity, we assume only $y$ direction component is non-zero KK expansion

$$V_y = v(z)e^{-ik\cdot x}. \tag{2.26}$$

The equation of motion is

$$\frac{d}{dz}\left(\frac{1}{z}\frac{d}{dz}v(z)\right) - \frac{k^2}{z}v(z) = 0 \tag{2.27}$$

which becomes where

$$v(z) = \sqrt{z}\psi(z). \tag{2.28}$$

Using $\psi(z)$ defined by the following equation of the form of the Schröodinger equation

$$-\frac{d^2}{dz^2}\psi(z) + \frac{3}{4z^2}\psi(z) = -k^2\psi(z) \tag{2.29}$$

The normalizable mode that this equation has corresponds to the operator of the meson, and $-k^2$ can be interpreted as its mass spectrum. And since the normalizable mode has solutions only for discrete values of $-k^2 = m_n^2$, we know that the meson spectrum is discrete. Since the potential term vanishes at $z \to \infty$, if we denote the excited levels by a positive integer $n$, the behavior of the spectrum $m_n^2$ at $n \gg 1$ is

$$m_n^2 \sim n^2 \tag{2.30}$$

On the other hand, in the meson spectra observed in hadron experiments, it is known that the square of the mass is rather linear with respect to $n$. The following soft wall model solves this contradiction.

### 2.2.2 Soft wall model

The linearity of the spectra of the excited states of the meson is called the Regge locus; the Regge locus appears in the data from hadron experiments, where the square of the mass increases linearly with respect to the excited level and spin. (Figure2.1). Below we review the soft wall model, a model that reproduces this well.

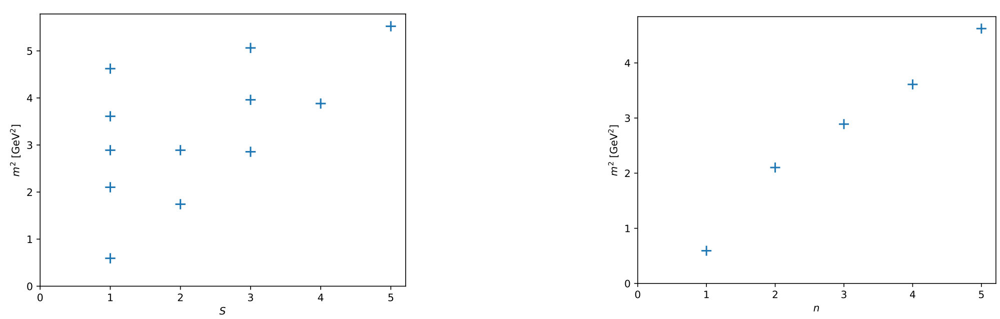


Figure 2.1: Left: Spectrum of a meson as observed by the Hadron experiment. The horizontal axis represents the spin of the meson, and the vertical axis is the mass squared. The plot is made using the central value of the observation and is based on [24]. The linearity of the mass squared $m^2$ with respect to spin is confirmed. Right: Plot of $rho$-meson spectra. Linearity with respect to the excited level $n$ can also be confirmed.

In the soft wall model, we consider a dilaton field $\Phi(z)$ in addition to the gravity field $g_{\mu\nu}(z)$ as a background field. We assume that the dilaton field is not constant but depends on the five-dimensional radial coordinate $z$ and increases with $z^2$. By using such a dilaton field, instead of introducing a cutoff in spacetime, we introduce a smooth wall in spacetime [9]. Since there is no cutoff, the metric is a five-dimensional AdS spacetime.

$$g_{MN}dx^M dx^N = e^{2A(z)}\left(dz^2 + \eta_{\mu\nu}dx^\mu dx^\nu\right) \tag{2.31}$$
$$= \frac{1}{z^2}\left(dz^2 + \eta_{\mu\nu}dx^\mu dx^\nu\right) \tag{2.32}$$

The function $A(z) = -\log z$ is introduced here because, as we will see later, only the linear combination of $\Phi(z)$ and $A(z)$ works for deriving the spectrum. Also, the spacetime is AdS, but scale symmetry is broken by the dilaton field.

Let us calculate the spectrum of the $\rho$ meson as in the hard wall model, and we will use the same gauge fixing condition as in the hard wall model, (2.23), to write down the effective action of the bulk field.

$$I_{\text{vector}} = -\frac{1}{4g_5^2}\int dz d^4x e^{-\Phi}\sqrt{-g}(F_{MN})^2 \tag{2.33}$$
$$= -\frac{1}{4g_5^2}\int dz d^4x \sqrt{-g}e^{-\Phi}g^{zz}g^{\mu\nu}\left(\partial_z V_\mu \partial_z V_\nu - 2V_\mu \partial^2 V_\nu\right) \tag{2.34}$$
$$= -\frac{1}{4g_5^2}\int dz d^4x e^{A-\Phi}\Big(\partial_z V_\mu \partial_z V^\mu - 2V_\mu \partial^2 V^\mu\Big). \tag{2.35}$$

However, again, for simplicity, only one flavor is considered here, using flavor symmetry. Also, the function $B$ is defined as

$$B(z) \equiv \Phi(z) - A(z) = z^2 + \log z \tag{2.36}$$

The equation of motion derived from this action under the KK expansion (2.26) is as follows.

$$\frac{d}{dz}\left(e^{-B(z)}\frac{d}{dz}v(z)\right) + m^2 e^{-B}v(z) = 0 \tag{2.37}$$

Furthermore, instead of finding $v_n$ directly, replace

$$v_n = e^{B/2}\psi_n \tag{2.38}$$

the equation still returns to the form of the Schr"odinger equation.

$$\left[-\frac{d^2}{dz^2} + V(z)\right]\psi_n = m_n^2\psi_n \tag{2.39}$$

The potential term is

$$V(z) = \frac{B'^2}{4} - \frac{B''}{2} = z^2 + \frac{3}{4z^2}. \tag{2.40}$$

The analytic solution for (2.39) is known; using Laguerre polynomial $L_n^m$ to write down the solution

$$\psi_n(z) = \sqrt{\frac{2n!}{(n+1)!}} e^{-z^2/2} z^{\frac{3}{2}} L_n^1(z^2). \tag{2.41}$$

The eigenvalue for this solution is

$$m_n^2 = 4(n+1). \tag{2.42}$$

This is just the same spectrum as the Regge trajectory.

The linear spectrum was obtained, after all, because the model was based on the reasoning of the quantum mechanical system of harmonic oscillators. As a result of fixing the dilaton field at $z^2$, the potential (2.40) of the equation giving the spectrum is effectively consistent with the harmonic oscillator system in a sufficiently large region of $z$.

### 2.2.3 Higer spin meson

By considering a soft wall model involving mesons with general spin, linearity with respect to the spin can also be derived [9]. When considering mesons of spin $S$, the bulk field is a (fully symmetric) tensor field of rank $S$. Relevant terms in the action of higher spin soft wall model are

$$I = \frac{1}{2}\int dx^5 \sqrt{-g} e^{\Phi} \left[ \boldsymbol{\nabla}_N \phi_{M_1 \dots M_S} \boldsymbol{\nabla}^N \phi^{M_1 \dots M_S} + M^2(z) \phi_{M_1 \dots M_S} \phi^{M_1 \dots M_S} \right], \tag{2.43}$$

where $M^2$ is the mass of the bulk field. Adopting $\phi_{z \dots} = 0$ as the gauge fixing condition and using the rescaled field $\phi_{\dots} = e^{2(S-1)A(z)} \tilde{\phi}_{\dots}$, this action is attributed to the massless form.

$$I = \frac{1}{2}\int dx^5 e^{5A-\Phi} \left[ e^{4(S-1)A} e^{-2A(1+S)} \partial_N \tilde{\phi}_{\mu_1 \dots \mu_S} \partial_N \tilde{\phi}_{\mu_1 \dots \mu_S} \right]. \tag{2.44}$$

Thus, the equation of motion for $\tilde{\phi}$ can also be written in the form of the Schr”odinger equation for (2.39), as in the $\rho$ meson. However, the spin dependence appears in the function $B(z)$ as follows.

$$B(z) = \Phi(z) - (2S-1)A(z) \tag{2.45}$$

and the potential term in (2.39) is

$$V_S(z) = z^2 + 2(S-1) + \frac{S^2 - \frac{1}{4}}{z^2}. \tag{2.46}$$

Since the second term is a constant shift with respect to the potential, it is ultimately included in the energy eigenvalues of (2.39) and has $S$-dependence as a spectrum. In fact, the Schr"odinger equation in the present case can also be solved rigorously, and the spectrum of the meson of spin $S$ is obtained

$$m_{n,S} = 4(n+S). \tag{2.47}$$

We will use this spin dependence of $B(z)$ to identify the spacetime metric and dilaton field separately later. Namely, once $B$ is determined for both $S = 1, 2$ then metric and dilaton are derived respectively.

$$A = (B_{S=1} - B_{S=2})/2 \tag{2.48}$$

$$\Phi = (3B_{S=1} - B_{S=2})/2 \tag{2.49}$$

## 2.3 Basics of deep learning

We would like to end the section reviewing basic contents with machine learning. T.M.Mitchel, the author of *"Machine Learning"*, give the definition for a machine learning algorithm as

"A computer program is said to learn from experience $E$ with respect to some class of tasks $T$ and performance measure $P$, if its performance at tasks in $T$, as measured by $P$, improves with experience $E$."

The simplest learning is linear regression. Let $\boldsymbol{x}, \boldsymbol{y}$ be $d$-dimensional real vectors. As a model to give output $\boldsymbol{y}$ for input $\boldsymbol{x}$, a linear model

$$\boldsymbol{y} = a\boldsymbol{x} + b. \tag{2.50}$$

In order to optimize the two parameters $a, b$ let us define a function and $\theta$ be a series of parameters of that function

$$\boldsymbol{y} = F(\boldsymbol{x}; \theta). \tag{2.51}$$

and optimize $\theta$.

Deep learning is one of the most successive frameworks of machine learning. By combining a model with 'depth' and an algorithm to optimize it, a model with high expressive power can be learned. The framework used in this dissertation uses a model called a neural network (Abbreviated as NN).

$$\boldsymbol{y} = \sigma\big(W^{(N)}\sigma\big(W^{(N-1)}\sigma\big(\cdots\sigma\big(W^{(1)}\vec{\boldsymbol{x}}\big)\big)\big)\big). \tag{2.52}$$

where $N$ is a natural number, $W^{(l)}$ is a orthogonal matrix, and $\sigma$ is a suitable nonlinear function $\sigma : \mathbb{R}^n \to \mathbb{R}^n$. Briefly, in this model, linear transformations by $W$ and nonlinear transformations by $\sigma$ are alternately applied to the input. one set of linear and nonlinear transformations is called a layer, and a model consisting of multiple layers is called a deep neural network (DNN). Deep Neural Network (DNN).

Learning algorithms using NNs can be broadly classified into three categories: supervised learning, unsupervised learning, and reinforcement learning. In supervised learning, the parameters of the model are adjusted with the aim that the output $\boldsymbol{y}$ of the model is closer for the input $\boldsymbol{x}$ to the known correct data $\boldsymbol{y}'$. As the distance between $\boldsymbol{y}$ and $\boldsymbol{y}'$ we define

$$E(\boldsymbol{y}' - \boldsymbol{y}) = \sum_{i}^{d} \frac{1}{d} \left| y_i' - y_i\big(\boldsymbol{x}; W^{(l)}\big) \right| \tag{2.53}$$

Then the optimization of the parameters of the supervised learning model is achieved by minimizing this function $E$.

Such a measure is called a loss function, and in particular, a function $E$ of the form (2.53) is called an L1 loss function. The gradient descent method described below is often used for parameter optimization; the

If the parameters of the DNN are $W_t$, and $E_t$ is the result of calculating the loss function by finding the output of the DNN, then

$$W_{t-1} = W_t - \eta \frac{\partial E_t}{\partial W_t} \tag{2.54}$$

The parameters are updated by where $\eta$ is usually a small positive real number and is called the learning rate. By repeating this update, the parameters are adjusted little by little so that $\frac{\partial E_t}{\partial W_t}$ becomes zero.

The gradient descent method is a simple method, but loss functions are generally multivariate functions, and many minimum points are expected to exist. If ideal data are available, finding the minimum point will most likely improve the performance of the model, but sometimes the parameters stop updating at a minimum point that is not the minimum point. To avoid such a situation, parameters such as the learning rate, the number of layers in the DNN, and the size of the $W$ matrix (= number of parameters per layer twin) must be appropriately adjusted by humans in advance. These values are called hyperparameters. Another method often used is to add a regularization term to the loss function that imposes arbitrary restrictions on the learning parameters, thereby changing the shape of the function and avoiding a minimum point.

# 3 Constructing background field in AdS/QCD model from meson spectrum

In this section, we upgrade the deep neural network given in Refs. [5, 6] to accommodate hadron two-point functions as a supervised learning and use the experimental data of the mass of $\rho$ mesons and $a_2$ mesons at zero temperature as the training data. The neural network is a discretized bulk action of the AdS/QCD model [7, 8, 9], with the metric and the dilaton fields identified as the network weights. With some physically reasonable regularization, the supervised learning of the neural network is successful, ending up with smooth profiles of the gravity metric and the dilaton configuration in 5 spacetime dimensions, as the trained weight parameters of the neural network. Namely, the inverse problem of finding the gravity system for a given hadron spectra is solved by the deep learning. Using the obtained metric and dilaton, we can predict excited hadron masses which were not used as the training data.

The advantage of the deep learning method is that it can provide a systematic approach to determine the gravity dual from a given dataset of the QFT correlators, which even generalizes for prediction. Using the data analysis methods of deep learning [25], we may hope to combine all possible information of QCD as the training data to discover a proper gravity dual. For that, various QCD requirements studied in improved holographic QCD [26, 27] will help.

Let us focus on the vector meson sector in a AdS/QCD model. The gravity side is the 5-dimensional effective action of a $U(1)$ gauge theory

$$I_{\text{vector}} = -\frac{1}{4g_5^2}\int dz d^4x e^{-\Phi(z)}\sqrt{-g}F_{MN}F^{MN}\,, \tag{3.1}$$

where $F_{MN}$ is the field strength of the 5-dimensional massless gauge field $V_M(z, x^\mu)$, and $g_5$ is the gauge coupling constant. The indices $M, N$ represent those of the 5-dimensional spacetime, while the directions along the 4 dimensions associated with QCD are denoted as $\mu, \nu$. The emergent 5-th direction is parameterized by the coordinate $z$ ($\geq 0$). Everything is made dimensionless by using the AdS radius $L$.

The theory is in a curved spacetime. The soft wall models include the gravity metric $g_{MN}(z)$ and the dilaton field $\Phi(z)$ as the background fields. In particular, the dilaton field is essential in the spectral analyses in Ref. [9]. The metric is written with a single function $A(z)$ without losing its generality,

$$g_{MN}dx^M dx^N = e^{2A(z)}\left(dz^2 + \eta_{\mu\nu}dx^\mu dx^\nu\right)\,, \tag{3.2}$$

because QCD is in an infinitely extended flat Lorentzian spacetime, at zero temperature. For the use of the AdS/CFT correspondence, it is assumed that the curved spacetime is asymptotically AdS: $A(z) \sim -\log z$ near the AdS boundary $z = 0$, where the unit $L = 1$ is used.

Following Ref. [9], we choose a gauge $V^z = 0, \partial_\mu V^\mu = 0$. Using the plane wave basis for the 4 dimensions, we consider a solution of the form

$$V^\mu(z, x^\mu) = v(z) c^\mu e^{-ikx}\,, \tag{3.3}$$

with a mass-shell condition $-k^2 = m^2$ for the 4-dimensional mass $m$. Then we obtain the following equation which the coefficient function $v(z)$ should satisfy,

$$\frac{d}{dz}\left(e^{-B(z)} \frac{d}{dz} v(z)\right) + m^2 e^{-B(z)} v(z) = 0\,. \tag{3.4}$$

Here we have defined the combination

$$B(z) \equiv \Phi(z) - A(z)\,. \tag{3.5}$$

In the AdS/CFT dictionary, for the current operator of QCD to be excited, the corresponding modes in the gravity side need to be normalizable. The differential equation (3.4) has normalizable solutions only for discrete values of the mass $m = m_n$ ($n = 0, 1, 2, \cdots$). Therefore, these discrete values $m_n$ are interpreted as the vector meson spectrum.

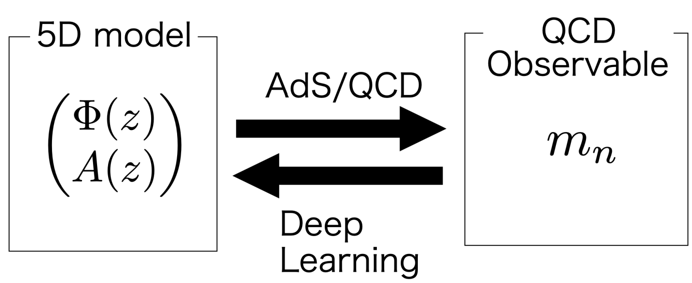


Figure 3.1: In the ordinary AdS/QCD modeling, one prepares the background metric and dilaton fields ($A(z)$ and $\Phi(z)$) and then calculates the QCD observables (the hadron mass $m_n$). The judgement of whether the chosen background is appropriate is checked after matching the calculated observables with experimental data. On the other hand, our AdS/DL approach solves backward.

So, summarizing the procedures, once the explicit form of the metric function $A(z)$ and the dilaton profile $\Phi(z)$ is given, one can calculate the normalizable solutions of (3.4) to obtain the vector meson mass spectra. See Fig. 3.1 for the illustration. In Ref. [9] the following functions are used,

$$A(z) = -\log z\,, \quad \Phi(z) = z^2\,. \tag{3.6}$$

This ansatz is simple enough since $A(z) = -\log z$ means that the whole 5-dimensional spacetime is $AdS_5$, and $\Phi(z) = z^2$ was adopted to produce the asymptotic Regge behavior in the hadron spectra.

One can also calculate the spectra of higher spin mesons from the 5-dimensional model. A spin-$S$ meson is dual to a rank-$S$ symmetric tensor field [28]. By the procedures similar to those of the vector meson case, the $z$-dependent part of the bulk tensor field obeys the same equation as (3.4) with a different definition of $B(z)$;

$$B(z) = \Phi(z) - (2S - 1)A(z). \tag{3.7}$$

One understands that the spin dependence of the meson spectra is encoded in the background bulk field profiles.

Now, one can see that the difficulty of the AdS/QCD model building is in solving inversely the duality: the direction of the standard procedures is only from the gravity to QCD quantities. One needs the explicit metric and the dilaton which are not known a priori.[2]

On the other hand, we aim at "optimizing" the model by experimental data. More concretely, we determine the model background $B(z)$ by using deep learning of the training data of hadron masses. See Fig. 3.1. In addition, using the spin dependence of the definition of $B(z)$ in (3.7), we can obtain the spacetime metric and the dilaton separately: the machine finds different $B(z)$'s from the data for the mesons with $S = 1$ and $S = 2$ respectively, then the metric and the dilaton are obtained as

$$A(z) = (B_{S=1} - B_{S=2})/2\,, \tag{3.8}$$

$$\Phi(z) = (3B_{S=1} - B_{S=2})/2\,. \tag{3.9}$$

Using these, one can calculate other QCD observables as a prediction of the determined model. Our proposal offers a new data-driven approach to the AdS/QCD model building.

## 3.1 Neural network for AdS/QCD

In this section we construct our neural network. According to the concept of the AdS/DL correspondence [5], we present a deep neural network architecture optimizing

[2]One can of course resort to Einstein dilaton equations of motion assumed, to constrain possible profiles of the metric and the dilaton fields, see Refs. [26, 27]. A partial list of the obstacles are (i) dilaton potential allows arbitrariness, (ii) since QCD is $N = 3$ quantum gravity corrections such as higher derivatives in curvatures may exist, and (iii) string theory effective action is too restrictive at tree level while generic quantum gravity corrections are unknown.

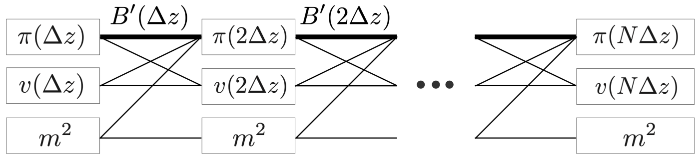


Figure 3.2: Neural network representation of (3.12). The layer depth direction (horizontal direction in this figure) corresponds to the emergent radial direction of the 5-dimensional spacetime. The input is on the left, the output is on the right. Only the thick lines are trainable weights, corresponding to the bulk background field $B'(z)$. The binary classification layer at the output is not shown in this figure, for simplicity.

a generic soft-wall AdS/QCD model. The optimization is conducted under a supervised deep learning, with respect to the QCD experimental data, where the meson spectrum $m$ in (3.4) is treated as the input data.

The implementation can be divided into three steps. First, we translate the equation of motion (EOM) of the bulk field into a deep neural network. The network itself is regarded as a spacetime, and the metric on the discretized spacetime corresponds to trainable weight parameters in the neural network. The next step is to arrange the input and the output layers for a binary classification. The input data is the vector meson spectrum data, and the output data is related to the normalizability condition of the solution of the bulk field equation. The remaining step is technical for the training to be successful: fixing hyperparameters and introducing a regularization. We must adjust the value of the hyperparameters such as the discretization spacing and the number of layers. We also need a regularization which come from physical requirements such as smoothness of the spacetime. In the following, in each subsection we explain the three steps described above.

### 3.1.1 Deep neural network

We prepare a deep neural network where trainable weight parameters are identified with the configuration of the gravity/dilaton fields of the holographic model. We identify the radial propagation (3.4) of the bulk vector field from $z$ to $z + \Delta z$ with the propagation of the information on the neural network from one layer to another.

We introduce a conjugate momentum field

$$\pi(z) \equiv \frac{\partial}{\partial z} v(z) \tag{3.10}$$

to reduce (3.4) to a set of first order differential equations, one of which is

$$\begin{aligned} 0 =& \frac{\partial}{\partial z}\Big(e^{-B(z)}\pi(z)\Big) + m^2 e^{-B(z)} v(z) \\ =& e^{-B(z)}\left[-B'(z)\pi(z) + \pi'(z) + m^2 v(z)\right] . \end{aligned} \tag{3.11}$$

Then we discretize the $z$ coordinate in (3.10) and (3.11) with a spacing $\Delta z$,

$$\begin{cases} \pi(z+\Delta z) & = \pi(z) + \Delta z\,(B'(z)\pi(z) - m^2 v(z)) \\ v(z+\Delta z) & = v(z) + \Delta z\,\pi(z) \end{cases} \tag{3.12}$$

The derivatives acting on the vector field $\pi$ and $v$ are replaced by the difference, and we leave the form $B'(z) \equiv \partial B/\partial z$ as it is.

With this (3.12), let us make a neural network representation of the bulk field equation. The propagation equation (3.12) tells us that the values of $(\pi, v)$ at $z = N\Delta z$ with an integer $N$ can be computed from the initial values of $(\pi, v)$ at $z = \Delta z$ and $m$, when a background $B'(z)$ is given. Namely, the output of the system is given by the input and $B'(z)$,

$$\begin{pmatrix} \pi(N\Delta z) \\ v(N\Delta z) \end{pmatrix} = F\Big(\pi(\Delta z), v(\Delta z), m; B'(z)\Big) . \tag{3.13}$$

Recall that in a generic feedforward deep neural network (DNN) the unit values at the final layer are calculated by the unit values at the initial layer with a given trainable weights. The concept of the AdS/DL correspondence is based on this similarity [5]. Following that, we find the dictionary between the bulk field equation and the neural network as shown in TABLE 3.1.

| EOM | DNN |
|---|---|
| $z$ | layer label |
| $B'(z)$ | weights |
| $\pi(z), v(z), m$ | units |
| $F$ | architecture |

Table 3.1: The relationship of between the EOM (3.11) and the DNN. Here $m$ is $z$-independent in (3.11), so it corresponds to a unit of a fixed value.

Equation (3.13) is nothing but the deep neural network itself, with the layer depth direction identified as the emergent radial direction $z$. See FIG. 3.2. The AdS boundary $z = 0$ is identified with the input layer, while the deep infrared region of the emergent space $z = \infty$ is the output layer. Generically, neural network weights are matrix-valued trainable parameters, while our weights include only $B'(z)$ as the trainable parameters. This means that our neural network is sparse, and most of weight components are put to 0 or some fixed value.

As we mentioned, the 5-dimensional spacetime is asymptotically $\mathrm{AdS}_5$ near $z = 0$, so we can determine the values of $(\pi, v)$ at the initial layer $z = \Delta z$, based on their behavior in the AdS. Using the asymptotic solution of (3.4) with the AdS metric (and assuming that the dilaton vanishes there), we find

$$\pi(\Delta z) = 2S(\Delta z)^{2S-1}\,, \quad v(\Delta z) = (\Delta z)^{2S}\,. \tag{3.14}$$

See App. A.1 for the derivation. The overall proportionality magnitude of $v$ and $\pi$ is ignored since the EOM (3.4) is linear in $v(z)$. See FIG. 3.2 for the whole schematic view of our neural network.

### 3.1.2 Dataset for binary classification

The next step is to prepare training dataset for our supervised leaning. Since we want to extract possible features from the experimental data of the meson spectrum, we may simply use the value of the spectrum as our input. Then, what should the output data be? In view of (3.13), the output data is the values of the vector field at $z = \infty$. Depending on whether the mode $v(z)$ is normalizable or not, the values of $v(z)$ at large $z$ vanish or diverges. It needs to be normalizable only when we have the correct value of the input mass $m$. In this way, we can arrange the neural network as a binary classification problem, by putting a discrimination label to the input mass.

More concretely, as the input data we prepare a set of random real numbers (the mass). The range of the generated random numbers include the experimentally measured values of the meson mass. If the random number is close to (far from) the experimental values in the real spectrum, it is named as a positive (negative) data. In the training data, the output value as the label for the positive (negative) data should be 0 (1), which is the discrimination label. Therefore, we give our neural network a task to classify the input real numbers: a meson mass classifier.

Since we expect the final output to be 0 or 1, we introduce an additional layer there. This layer outputs 0 or 1 according to whether the value of $v(N\Delta z)$ satisfies the following normalizability condition or not,

$$v(N\Delta z)e^{-B(N\Delta z)/2} \le \epsilon\,. \tag{3.15}$$

For this, we arrange as the final layer a smeared box function of the width $\epsilon$, with no weight multiplication.[3] And as for the loss function, we simply adopt L1 loss.

### 3.1.3 Hyperparameters and regularization

For the machine learning to work, we must tune the hyperparameters in the architecture, and we need to introduce regularization terms to the loss function.

Our hyperparameters are, the number of layers $N$, and the discretization spacing $\Delta z$ which appears in the fixed weights of the neural network,[4] and the discrimination threshold $\epsilon$ in (3.15) in the classification layer. In fact, these are closely related to each other from a physical viewpoint, as follows.

First, $N$ and $\Delta z$ give the location $z = N\Delta z$ at which whether the vector field $v(z)$ behaves as a normalizable function or not is verified. The threshold for the discrimination is $\epsilon$. Although in principle we have $\epsilon \to 0$ for $N \to \infty$, for our numerical calculations we need a finite $N$. In addition, even though the analytic solution goes to 0 at $z \to \infty$, due to the discretization error of the differential equation (3.4) the value at $z = N\Delta z$ could deviate from 0. So, for the network to work properly even with the discretization effect, we need to tune $\epsilon$ such that it also allows the deviation. In practice, we fix these hyperparameters by using the analytic solutions in the famous soft wall model of Ref. [9], see App. A.2 for the details.

The regularization which should be added to the loss function is introduced by the following three reasons. The first one is the spacetime interpretability. The obtained set of weights is interpreted as $B(z)$, which is the dilaton field and the metric field. They need to be a smooth function of $z$, otherwise there is no physical interpretation [5, 6]. Second, as in (3.14), for the AdS/CFT to work, we impose the asymptotic AdS condition, which constrains the form of $B(z)$ near the initial layer, the boundary $z = 0$. The third reason is the soft wall. For (3.4) of the vector field to have normalizable solutions,[5] the background field needs to have an infrared wall. This is also related to the technical trainability of the neural network, and to the choice of the random initial

[3]Here, $\pi$ also needs to be normalizable for a positive data, but in our implementation we do not look at it. This is because $\pi$ is expected not to converge well at large $z$, due to discretization errors.

[4]There is an option to treat $\Delta z$ as additional trainable parameters. This $\Delta z$ could even depend on $z$. This training of the $z$-dependent spacing $\Delta z$ appears to be a quantum gravity, which is intriguing, and we leave the optimization of the spacing in AdS/DL to a future problem.

[5]The EOM (3.4) can be rewritten in the form of a Schrödinger equation (see Ref. [9]), and the potential of the Schrödinger equation depends only on derivatives of $B(z)$. In the model of Ref. [9] the background (3.6) corresponds to a harmonic oscillator potential at large $z$, which is the "wall" of a confining geometry. We introduce a regularization so that the machine can find a similar behavior.

configurations of $B'(z)$ before the training.

Therefore, we introduce the following three kinds of regularization terms:

- $B(z)$ is a smooth function of $z$.
- $B(z)$ is asymptotically AdS at small $z$.
- $B(z)$ has a "wall" at large $z$.

For concrete functional forms of these regularizations in the loss function, see App. A.3.

## 3.2 Optimization by the data of meson spectrum

In this section, we determine the background of the AdS/QCD model (3.1) by training our neural network with the dataset of the meson spectrum. We have two numerical experiments. The first one is a test case to check whether our deep learning can actually reproduce the soft wall model (3.6) of Ref. [9] from the data which is generated by the model with (3.6) in advance. We confirm that our architecture can learn the model successfully. The second numerical experiment is the optimization of the model by deep learning with the experimental data of the meson spectrum. The machine finds a metric function $A(z)$ and a dilaton profile $\Phi(z)$ which are consistent with the experimental data. We discuss physical implication of the determined AdS/QCD model.

### 3.2.1 Reproduction test

Since the implementation of our neural network is totally based on the generic soft wall model, as a first check of whether our architecture works properly, we perform a reproduction test of the model of Ref. [9] with (3.6). First, we prepare the mass spectra calculated by the model with (3.6). Then, using only that set of data, we train our neural network to find $B'(z)$. Then we compare the function $B'(z)$ which machine determined, and the function (3.6). If we confirm that they are similar enough, then we claim that our architecture works and the model of Ref. [9] is reproduced.

For the dataset of $m^2$, we generate a set of real numbers in the range $[0, 10)$. This range includes the first two levels of the spectrum, since the meson masses calculated by the model of Ref. [9] is $m_n^2 = 4(n+1)$ with $n = 0, 1, 2, \cdots$ (see Fig. 3(a)). Note that the widths of the region of the positive data (the blue dots in Fig. 3(a)) are chosen by hand, which are hyperparameters.

In FIG. 3.4, we show the result of our deep learning with $N = 20$, $\Delta z = 0.2$, $\epsilon = 0.25$, and 20 times of the repetition of the training. The result shows that the soft

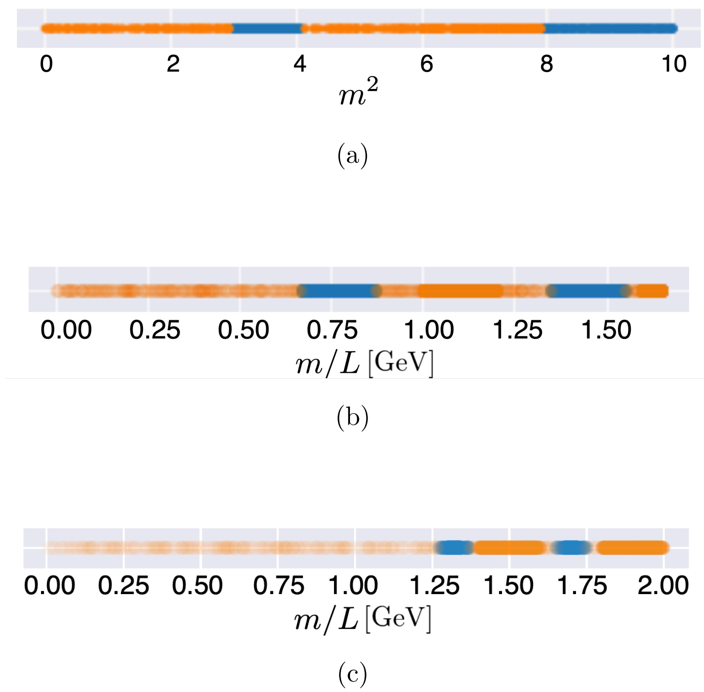


Figure 3.3: Visualization of the positive/negative datasets we use. Blue/orange points represent positive/negative data. The data (a) is for the spectrum $m^2$ of the model of Ref. [9] used in section 3.2.1, and the data (b) and (c) are for the spectra $m/L$ of the $\rho$ meson and for $a_2$ meson used in section 3.2.2, respectively.

wall model of Ref. [9] is reproduced well, qualitatively. Although we introduce some physical regularizations such as the asymptotic AdS condition and the wall condition, it is worth noted that only a part of the meson spectra is used for training the model. Hence, we claim that our deep learning architecture works for the meson spectrum as the input data. And in particular, the AdS/DL paradigm is shown to be helpful to construct effective AdS/QCD models.

### 3.2.2 Model determined by experimental data

Finally, we come to the actual aim of the deep learning method: the determination of the metric/dilaton functions by the experimental data of the meson spectra. We use the spectra of the $\rho$ meson ($S = 1$) and the $a_2$ meson ($S = 2$). Combining the results of these two, we can obtain $\Phi(z)$ and $A(z)$ separately, as shown in (3.7).

The experimental data of the tower of the $\rho$ meson spectrum [24] is given as $\rho(770)$, $\rho(1450)$, $\rho(1700)$, $\cdots$, and we use only the first two levels, since it is expected by the

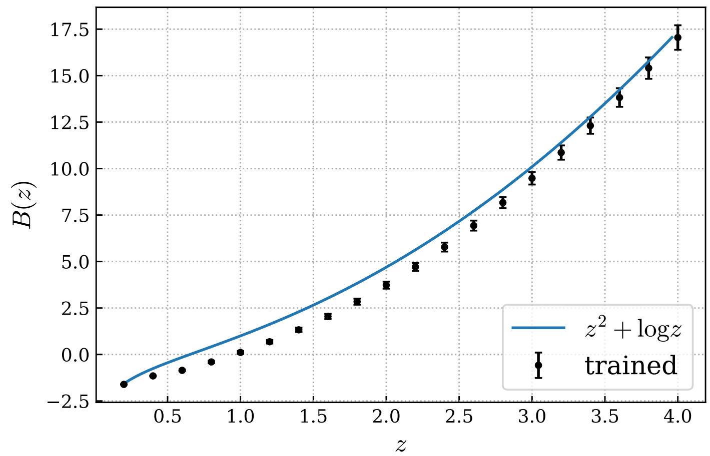


Figure 3.4: The trained result of the reproduction test, $B(z)$. The trained 20 functions $B'(z)$ (for 20 trainings) are averaged, then discretely integrated over $z$ to get $B(z)$, plotted with $2\sigma$ error bars. Blue curve represents the model of Ref. [9], $B(z) = \log z + z^2$ given in (3.6).

analysis of the model of Ref. [9] that the discretization errors are difficult to be handled for higher excitations. As for the $a_2$ meson, $a_2(1320)$, $a_2(1700)$ are reported as the established poles [24]. We generate the input data with these values and design our neural network. (See FIg. 3(b) and Fig. 3(c) for the generated input data, and TABLE 3.2 for the hyperparameters of the architecture. For details of the hyperparameters, the initial weights, and the dataset generation, see App. A.2, App. A.4, and App. A.5, respectively.)

| meson | $\Delta z$ | $N$ | $\epsilon$ | mass (GeV) | num. of input data |
|---|---|---|---|---|---|
| $\rho$ | 0.2 | 20 | 0.25 | 0.77, 1.45 | pos:2000/neg:2000 |
| $a_2$ | 0.05 | 80 | 0.25 | 1.32, 1.70 | pos:3000/neg:3000 |

Table 3.2: Hyperparameters and dataset we use. The values of the mass spectra are taken from Ref. [24].

In the implementation of the dimensionfull quantities (such as the masses) into the numerical experiment, we normalized everything appearing in (3.4) in the unit of the AdS radius $L$. It is actually the unique dimensionfull parameter in the simple AdS/QCD model (3.1). The input values in Fig. 3(b) and Fig. 3(c) are multiplied by $L$ when they are used in the training. The value of $L$ can be chosen arbitrarily, and here we choose it in such a way that the mass of the lowest $\rho$ meson (0.77GeV) is equal to the mass of the ground state ($m_n^2 = 4(n+1)$) of the model of Ref. [9] in the unit of $L$, for simplicity.

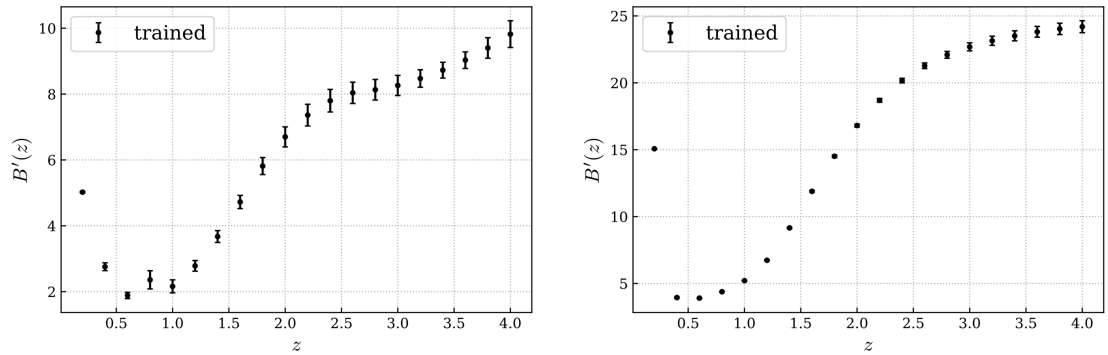


Figure 3.5: The trained result of $B'(z)$, for (a) $\rho$ meson and for (b) $a_2$ meson. The training is repeated twenty times and five times, respectively. The average values over the iteration are plotted. The error bars represent $2\sigma$.

[6] This results in $L = \sqrt{4/0.77^2} \sim 2.6\text{GeV}^{-1}$ as the unit of length.

We repeat the training of the neural networks with those dataset, twenty times for the $\rho$ meson and five times for the $a_2$ meson, separately. The network is optimized, and the emergent $B'(z)$s are obtained, which are shown in FIG. 3.5.

To obtain the metric and the dilaton, we calculate $B(z)$ by a discretized integration

$$B(z = n\Delta z) = \sum_{k=1}^{n} B'(k\Delta z)\Delta z + C\,. \tag{3.16}$$

We set the integration constant $C$ such that $B(\Delta z) = \log \Delta z$ because $B(z)$ should behave as an asymptotically AdS spacetime, $A(z) \simeq -\log z$ by the assumption. From this integral we compute the metric profile function $A(z)$ and the dilaton profile function $\Phi(z)$. They are shown in FIG. 3.6 and FIG. 3.7.

The emergent metric $A(z)$ for the near-boundary region $0 < z \leq 2.0$ can be consistently fit with a function

$$A(z) = -\log z + a_1(z-0.2) + a_2(z-0.2)^2 + a_3(z-0.2)^3\,, \tag{3.17}$$

with $a_1 = 0.849$, $a_2 = -0.496$, and $a_3 = -0.433$. The first term ($-\log z$) is for the $\text{AdS}_5$ spacetime, and the corrections are obtained as above. The fitting Taylor series

[6] Our neural network given in FIG. 3.2 is constructed based on the equation of motion for the model of Ref. [9], which includes no dimensionfull quantity, while we confirm this conducts the training successfully as shown in the reproduction test. To adopt the same architecture for the training with the hadron data, we normalize the mass spectra by $L$. The value of $L$, which we choose so that the scale of input value is as large as one of reproduction test case, can be also important for the training to be successful.

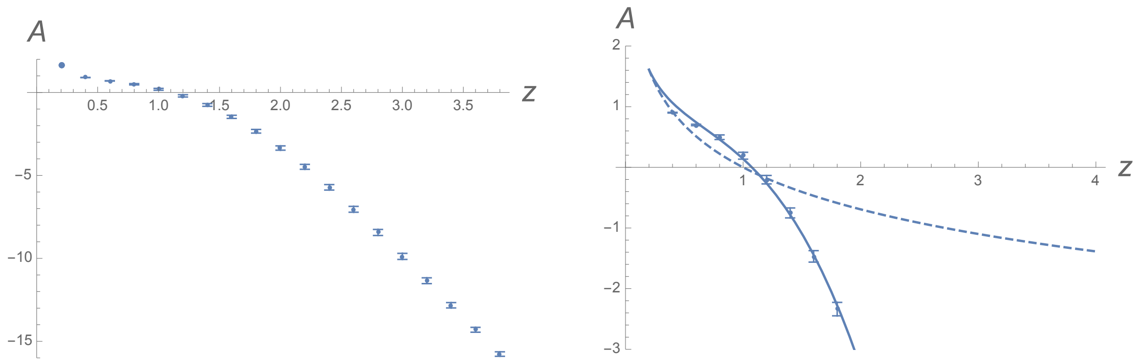


Figure 3.6: (a) Emergent metric function $A(z)$ with the statistical error bars. (b) Enlarged figure near the boundary, $z \sim 0$. The solid line is the fitting function (3.17). The dashed line is $-\log(z)$ which is the AdS spacetime.

for the deviation from the AdS is in the power of $(z - 0.2)$ where $z = \Delta z = 0.2$ is the location of the initial layer. [7]

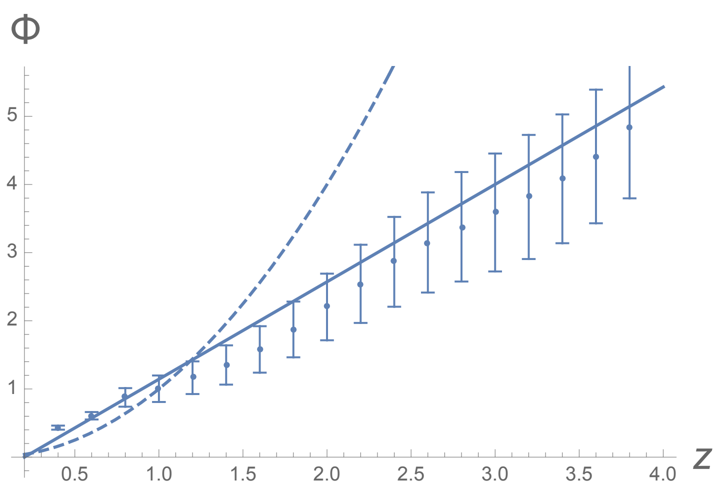


Figure 3.7: Emergent dilaton profile. The solid line is a fit (3.18), and the dashed line is $\Phi = z^2$ of the model [9].

The emergent dilaton profile is plotted in Fig. 3.7. The obtained points with the error bars can be fit well with a linear function,

$$\Phi(z) = \phi_1(z - 0.2) \tag{3.18}$$

[7] The IR parts of FIG. 3.2.2 and FIG. 3.7 are not so reliable compared to the UV parts of them, simply because the meson wave functions are suppressed at the IR region and so less sensitive to the background metric and the dilaton. The obtained IR behavior could depend on our hyperparameters and regularization.

with a constant $\phi_1 = 1.43$. As one can see in Fig. 3.7, our deep learning has found a linear dilaton profile, rather than the $z^2$ behavior which was originally anticipated in Ref. [9]. The linear dilaton is a popular background in string theory as the world sheet theory is solvable, and it is interesting that it shows up in the machine learning.[8]

### 3.2.3 Physical properties of the emergent spacetime

With the optimized emergent metric and dilaton functions, we can even try to make a prediction. We calculate the mass of the next-higher level excitation of the $\rho$ meson and the $a_2$ meson. Numerically calculating the eigenvalue of (3.4) with our emergent $B(z)$, we summarize the result in TABLE 3.3.

| Meson | Model prediction (GeV) | Experiment (GeV) |
|---|---|---|
| $\rho$ | 1.52 | 1.70 |
| $a_2$ | 2.44 | - |

Table 3.3: Comparison of the experimentally measured spectra of the third-lowest excitation of $\rho$ and $a_2$ [24], with our prediction from the optimized AdS/QCD model on the emergent background.

In the middle column of TABLE 3.3, the calculated mass of the third-lowest excitation of each meson is shown. As for the $\rho$ meson, our optimized model predicts the mass which is compared with the experimental data within 10 percent error. Our prediction of the $a_2$ meson mass will be confirmed in future experiment, as there is no established value in experiments at present.

Our prediction accompanies a caution, as our architecture is based on various hyperparameters and discretization errors, as well as the fact that we only use the lowest and the second-lowest meson masses as the training data. A change in widths introduced in the positive/negative data in FIG. 3.3 may cause unsuccessful trainings. One of the deficits of deep learning in general is unknown relations between hyperparameters and generalization, and any prediction is with such a caution. Nevertheless, we find that our prediction is still reasonable, which is encouraging.

Finally, let us discuss the physical property of the emergent metric (3.17) and the dilaton (3.18). Using these, we find an effective volume element $\sqrt{-g}e^{-\Phi}$ which is in

[8] In the context of holographic QCD the exact linearity may cause a problem of continuous glueball spectra [26]. Since we have not assumed a bulk gravity action which is necessary to argue the glueball spectra, we leave this issue for our future problem.

the action (3.1). Since the radial $z$-dependence of the volume element reflects physical properties of the geometry, we plot a logarithm of our optimized effective volume element $5A-\Phi$ in FIG. 3.8. In the figure, for a comparison, we plot the dashed line which is $5A-\Phi$ of the model of Ref. [9].

We notice that when $z$ is increased and goes to the infrared, our volume element gradually deviates in the positive direction once, compared to the AdS spacetime of Ref. [9]. This can be also seen from the fact that the first correction $a_1$ in (3.17) is positive, meaning that the AdS spacetime is deformed toward a slower warping. One possible interpretation is that this is a tendency toward a confining geometry, which is consistent with that the non-supersymmetric QCD is a confining theory at zero temperature.

Then, with a further increasing of $z$, our effective volume element goes below the AdS line. The resultant bump of the volume element as a function of $z$ resembles the machine-learned geometry of the AdS/DL model for the lattice data of the QCD chiral condensate [6], where at the finite temperature the emergent geometry consists of both the confining wall and the black hole horizon. Our geometry is trained with experimental meson spectra, while the one in Ref. [6] is with different QCD observables. Finding a unique geometry consistent with more QCD observables is a challenging problem.

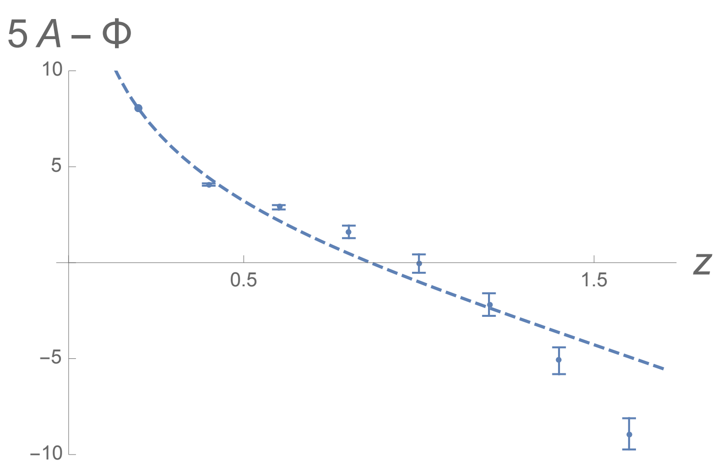


Figure 3.8: The logarithm of the volume element with the dilaton, $\log[\sqrt{-g}e^{-\Phi}] = 5A-\Phi$. The dashed line is that of Ref. [9], $5A-\Phi = -5\log z - z^2$.

We would like to make comments to the machine learning calculation. In our work, we have used only low-lying spectra of hadrons among the vast QCD spectral data, because of the following three reasons: First, the AdS/QCD approach is expected to be valid only at the strong coupling limit of QCD, *i.e.* in the low energy limit, thus only low-lying modes of light hadrons can be used with trust; Second, the experimental data of spectra of the higher excited hadrons may suffer from large decay widths while the linear AdS/QCD model do not describe the decay; Third, once the data of the higher modes is included, the training in the machine learning architecture used above does not work well. It would be interesting to explore a path to accommodate the spectra of the higher mesons and their decay widths. However, our concern is that the results of the $a_2$ meson training did not capture the characteristics of the data well: the training result could largely depend on the regularization imposed on the neural network. Thus, in this work we have decided to use only the result of the training with the spectrum of $\rho$ meson, thus only a single $B'(z)$, and we will reveal the profiles of the dilaton field and the metric by the further study described in following section.

# 4 Deriving dilaton potential in improved holographic QCD I

We present a method to derive the dilaton potential from the QCD observable data. We use the profiles of the background gravitational fields determined so that the bulk probe field fluctuation can reproduce the QCD observable data. The profiles are regarded as a solution of the Einstein equations. This requirement derives the dilaton potential backwards. As for the gravitational field profiles determined from the data, we can use the results using machine learning [15]. It is important that the dilaton potential can be derived in a data-driven manner.

In the machine learning calculation [15], the zero-temperature holographic model is characterized by two background fields, the metric and dilaton fields, and their properties are determined by the consistency with the meson spectrum. The line element is parametrized as

$$ds^2 = e^{2A(z)}\big(dz^2 + \eta_{\mu\nu}dx^\mu dx^\nu\big). \tag{4.1}$$

In this soft wall model, a useful combination of $A(z)$ and the dilaton field $\Phi(z)$ is

$$B(z) \equiv \Phi(z) - A(z). \tag{4.2}$$

The vector meson spectrum is calculated by solving the equation of motion of a bulk probe massless vector field. Therefore, determining the optimized model for given meson spectra is a kind of inverse problems, and thus algorithms based on neural networks are useful with spectral data as their input. Once the vector field equation is written down in a discrete form, one can translate the components of the equation into the components of the neural network, especially the background fields into the network weights [5]. Here the weight is a quantity that can be optimized in training the neural network. In the present case, because the vector field equation includes the background fields only in the form of $B'(z)$, this $B'(z)$ is identified to weights. As a result of the machine learning with the $\rho$ meson spectrum as the training data, the explicit profile of $B'(z)$ is determined [15].

The purpose of this section is to derive a dilaton potential by this $B'(z)$ profile. The method is as follows. First, we write down the equations of motion including the dilaton potential. Since we are assuming a zero-temperature system as the spacetime, the gravitational field has only one degree of freedom. Together with the dilaton's degree of freedom, the Einstein-dilaton system has two degrees of freedom, so we can obtain two independent equations of motion. Since the dilaton potential is undecided, we first need to eliminate it from these two equations. Then we use the $B'(z)$ profile to reduce that equation to that of the dilaton only and solve it to obtain $\Phi(z)$. We substitute it into the equation including the potential, and finally derive the dilaton potential $V(\Phi)$.

At the end of this section, we investigate the physics described by the derived Einstein-dilaton system in the following two perspectives: the asymptotic form of the obtained potential and the holographic Wilson loop that can be calculated from the derived model.

## 4.1 Derivation of dilaton potential

We are going to study an Einstein-dilaton system in the five-dimensional spacetime with an undetermined dilaton potential. In this section, we determine the dilaton potential $V(\Phi)$ so that the $B'(z)$ profile given by the data of hadron spectra is a solution of the Einstein equations. In addition, we would like to investigate the IR asymptotic behavior of the dilaton potential in comparison to the standard IHQCD potential. We also find that the resultant metric function indicates that the QCD confinement can be described by the derived holographic model.

In a minimal approach of IHQCD, one starts with a five-dimensional Einstein-Hilbert action accompanying a dilaton sector. This includes a five-dimensional metric $g_{MN}$, which is dual to the stress tensor operator in QCD, and the dilaton field $\Phi$, which is associated with the gluon composite operator. The Einstein frame action is

$$S = c\int d^5x\sqrt{g}\Big(R - \frac{4}{3}g^{MN}\partial_M\Phi\partial_N\Phi + V(\Phi)\Big). \tag{4.3}$$

The overall constant $c$ is the gravitational constant which is irrelevant in our work. In the standard holographic model building, the dilaton potential $V(\Phi)$ is provided so that the resultant system or the geometry reproduces known properties in QCD. Specifically, the behavior of the potential at a large $\Phi$ region is known to be important to reproduce the Regge behavior of the glueball spectrum. According to [26, 27], when $\Phi$ is large $V(\Phi)$ should take the form up to an overall factor

$$V(\Phi) \sim e^{2Q\Phi}\Phi^P \tag{4.4}$$

with $P = 1/2$ and $Q = 2/3$.

We assume a five-dimensional asymptotically AdS spacetime as in the standard AdS/QCD approach. Since we are going to explore the system whose solution is a given explicit function $B(z)$ in (4.2), we should use the same gauge as that used in [15]:

$$ds^2 = e^{2A(z)-\frac{4}{3}\Phi(z)}\big(dz^2 + \eta_{\mu\nu}dx^\mu dx^\nu\big). \tag{4.5}$$

Note that this is the Einstein frame metric, equal to string frame metric (4.5) times $e^{-4\Phi/3}$. The coordinate $z$ is the direction transverse to the spacetime of the boundary, and everything is made dimensionless in the unit of the AdS radius $L$. As for the warp factor $A(z)$, we shall impose the following two conditions according to [15]. First, the UV cutoff is put at $z = z_c \equiv 0.2$ then the bulk region is restricted to $z \geq z_c$ in the following calculations. Second, as the asymptotic AdS condition, we shall set $A(z) = -\log z$ at $z = z_c$.

In the gauge (4.5), the Einstein equations for (4.3) consist of two independent equations:

$$\begin{cases} 6A'' + 6A'^2 - 8A'\Phi' - 4\Phi'' + 4\Phi'^2 - e^{2A-\frac{4}{3}\Phi}V = 0 \\ 12A'^2 - 16A'\Phi' + 4\Phi'^2 - e^{2A-\frac{4}{3}\Phi}V = 0. \end{cases} \tag{4.6}$$

Here we use primes to denote a derivative with respect to $z$. We should notice that one can derive one more equation of motion by variation of the action with respect to $\Phi$, though it turns out to be unnecessary because it is not independent. Note that we have only two degrees of freedom in the present model due to the metric assumption of (4.5).

Our goal is to find a dilaton potential $V$ as a function of $\Phi$. For some given configuration of $A$ or $\Phi$, one might determine the dilaton potential as a functional of $\Phi$. In our case, since we have the numerical information about $B'(z)$, we compute the potential $V(z)$ numerically and investigate the dependence on $\Phi$ by drawing $V$ against $\Phi$ with $z$ treated as a parameter.

| $p$ | 0 | 1 | 2 | 3 | 4 | 5 |
|---|---|---|---|---|---|---|
| $a_p$ | 8.702 | -22.928 | 24.504 | -9.726 | 1.670 | -0.102 |

Table 4.1: List of coefficients for the polynomials in (4.7)

More precisely the numerical information is the value of $B'(z) \equiv \Phi'(z) - A'(z)$ at each discrete point on the $z$ axis. In order to proceed, we fit those values to a smooth function. The simplest choice is a polynomial. The fifth order polynomial fits those values well,

$$B'(z) = \sum_{p=0}^{5} a_p z^p \tag{4.7}$$

with the coefficients shown in TAB. 4.1.

Eliminating the unknown potential $V$ from (4.6) and using (4.2), we obtain a differential equation for the dilaton field:

$$\Phi'' = -\Phi'^2 - 2B'\Phi' + 3B'^2 + 3B''. \tag{4.8}$$

Since this is a non-linear equation, we carry out a numerical method for solving this equation. Here we simply integrate the equation step by step from the UV cutoff. The initial condition for $\Phi'$ should be $\Phi'(z_c) = 0$ because it was employed in [15]. On the other hand, the initial condition for $\Phi$ is arbitrary. So, we name $\Phi_c \equiv \Phi(z_c)$ and treat it as a free parameter below.[9]

We would like to mention how we calculate $B = \Phi - A$. Obviously $B$ can be obtained by integrating $B'(z)$, but a subtle point is its integration constant. To ensure $B(z_c) = \Phi(z_c) - A(z_c)$, we define $B(z)$ as

$$B(z) \equiv \int_{z_c}^{z} B'(\tilde{z})d\tilde{z} + \Phi_c + \log(z_c), \tag{4.9}$$

where $A(z_c)$ is set to $-\log(z_c)$ by the asymptotic AdS condition.

[9]In the standard IHQCD the dilaton goes to minus infinity ($\lambda = e^{\Phi} \to 0$) at the UV boundary while we introduce the UV cutoff at $z = z_c$. To get the precise UV behavior we must investigate $B(z)$ more rigorously.

Finally, we evaluate the dilaton potential. From (4.6) and $B'(z) = \Phi'(z) - A'(z)$, the potential can be written as follows:

$$V = 4e^{-\frac{2}{3}\Phi+2B}\big(-2B'\Phi' + 3B'^2\big). \tag{4.10}$$

Combining this with (4.7) and $\Phi(z)$ obtained from (4.8) leads to find $V(z)$. Then, by plotting $V$ against $\Phi$ with $z$ being a parameter, we finally obtain $V(\Phi)$. Its plot is shown in FIG. 4.1.

Potential fitting for the comparison between our obtained potential and various AdS/QCD models, here we provide a smooth analytic fitting the whole obtained plot. To make the fitting independent of $\Phi_c$, we use

$$\tilde{V} \equiv e^{-4\Phi_c/3}V, \quad X \equiv \Phi - \Phi_c. \tag{4.11}$$

Obviously, $\tilde{V}(X) = V(\Phi)$ for $\Phi_c = 0$ which is used in FIG. 4.1. Since we see that the growth of the obtained potential is mostly linear in the log plot, we can approximate its behavior with an exponential function. One candidate which can simultaneously also fit the part close to $X = 0$ is

$$\tilde{V} = 12\cosh(\gamma X). \tag{4.12}$$

and the best-fit value of the parameter is $\gamma = 1.433$. Interestingly, such a dilaton potential was used in [29] which provide the prediction to QCD quantities from an Einstein-dilaton system. [10]

Let us compare the derived potential with the one used in the IHQCD, (4.4). We shall perform a non-linear regression of $V(\Phi)$ with (4.4) and evaluate the values of

[10] As pointed out in [29], when one chooses the single hyperbolic cosine potential and considers the propagation of the dilaton field, $\gamma$ is bounded by the Breitenlohner-Freedman (BF) bound [30, 31] because the dilaton mass depends only on $\gamma$. Unfortunately, for our best-fit value of $\gamma$ in the case of (4.12), the dilaton mass breaks the bound. This motivates us to incorporate additional terms to avoid this problem, and one of the possible modifications is

$$\tilde{V} = 12\cosh(1.430X) - 16.778\ X^2 + 5.943\ X^4. \tag{4.13}$$

This also fits our numerical data well, while satisfies the BF bound.

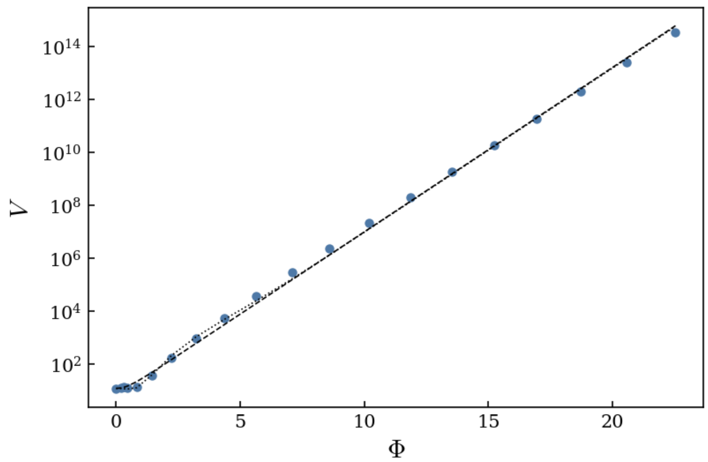


Figure 4.1: Plot of $V(\Phi)$ in a log scale. The dashed line and dotted line represents (4.12) and (4.13) individually. One can see that the exponential dependence on $\Phi$ is dominant at large $\Phi$.

$(P, Q)$. The subtle point is that $V(\Phi)$ has an ambiguity coming from $\Phi_c$. When $\Phi_c$ changes $V(\Phi)$ varies by some overall constant. Due to this ambiguity, the values of $(P, Q)$ depend on $\Phi_c$. So we calculate $(P, Q)$ for various initial values. The result when fitting $V$ to (4.4) in the range $1.4 \leq z \leq 2$ is shown in FIG. 4.2.[11] There are 200 points representing the values $(P, Q)$ with 200 independent $\Phi_c$'s. This plot shows there exists a pair of $(P, Q)$ which almost equals $(1/2, 2/3)$. The point is located at $P = 0.50,\ Q = 0.67$ and the corresponding value of $\Phi_c$ is -1.43.

Before ending this section, we study in detail the metric of the obtained model. In the way to calculate the dilaton potential, we have solved Einstein equation (4.3) with respect to the dilaton field. So now we are ready to find the spacetime metric itself instead of the combination $B(z)$. One can compute it by substituting the solution $\Phi(z)$ of (4.8) into the definition of $B(z)$. The result for $\Phi_c = 0$ is shown in FIG. 4.3.

It is remarkable that the string frame metric has a valley. As is well known, such a metric profile gives a confinement potential of the holographic Wilson loop [32, 33], and we shall study the Wilson loop in the next section. On the other hand, the Einstein frame metric does not have such a minimum. So the minimum is due to the dilaton field. Interestingly, this Einstein frame metric qualitatively matches that of the pure AdS metric. This result shows that the strange valley seen in the metric can be gravitationally consistent, as the phenomenon due to the frame difference.

[11] Having chosen this region is because 1) $\Phi$ needs to be large enough and 2) the deep learning result is reliable.

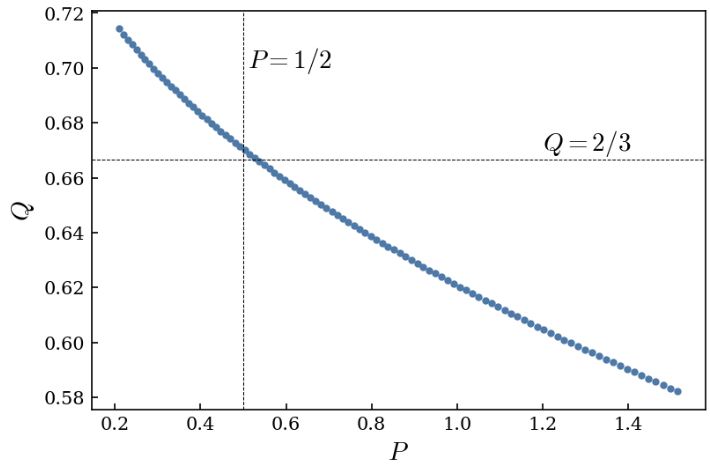


Figure 4.2: The values of $(P, Q)$. We use 200 initial values which divide [-2,0] into equal intervals. Each blue point corresponds to the result of regression with each of the initial values. As the initial value grows, $P$ tends to increase and $Q$ decreases.

For any future use of our numerical results, we express the numerically obtained metric as a continuous function. Because we assume that the metric becomes the pure AdS spacetime at $z \to 0$, we fit the plot with a function including a $1/z^2$ term. As we compared our potential with IHQCD potential, we focus on the region $z < 2$. One example of our fit results is

$$g_{zz}(z) = \frac{1}{z^2} + 1.917z^2. \tag{4.14}$$

This appears to approximate well the valley around the bottom $z \sim 1$.

## 4.2 Holographic Wilson loop

Once the dilaton potential in the IHQCD action is determined, one can perform holographic calculation of some QCD quantities from the action. In this section we calculate a holographic Wilson loop [32, 33] for the bulk spacetime metric in FIG. 4.3.

Let us consider a static fundamental string which hangs down from the boundary of the spacetime and lies in the bulk. Defining $z_0$ as the deepest point of the string in the direction of $z$, the quark-antiquark potential $E$ and the quark-antiquark distance $d$

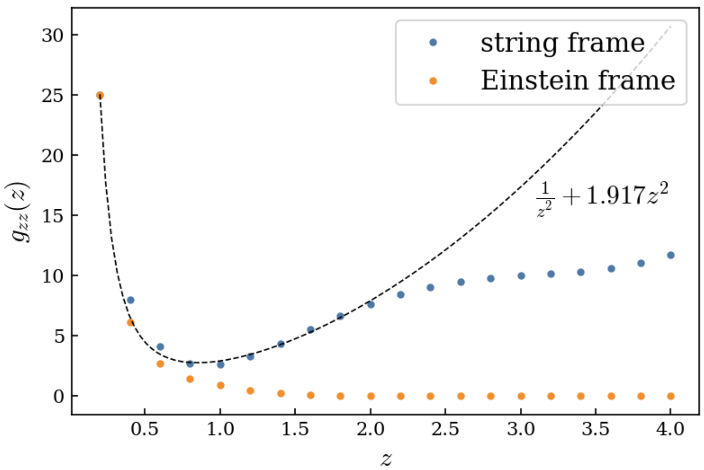


Figure 4.3: The metric obtained by solving (4.6) for our given $B(z)$. The string frame metric means $\exp(2A(z))$ and the Einstein frame metric corresponds to $\exp\bigl(2A(z) - \frac{4}{3}\Phi(z)\bigr)$. In this figure $\Phi_c$ is set to 0 just to make it easier to compare them. The dashed line represents (4.14).

are computed by the following integrals:

$$2\pi\alpha' E(z_0) = 2\int_0^{z_0} g_{zz}(z)\left(\sqrt{\frac{g_{zz}(z)^2}{g_{zz}(z)^2 - g_{zz}(z_0)^2}} - 1\right)dz \\ - 2\int_{z_0}^{\infty} g_{zz}(z)dz, \tag{4.15}$$

$$d(z_0) = 2\int_0^{z_0} \sqrt{\frac{g_{zz}(z_0)^2}{g_{zz}(z)^2 - g_{zz}(z_0)^2}}dz. \tag{4.16}$$

Here $\alpha'$ is the Regge slope parameter, and the gauge (4.1) is assumed. After eliminating $z_0$ from these two integrals, one can finally obtain $E(d)$, the quark potential.

The result for the determined holographic model FIG. 4.3 is shown in FIG. 4.4. The linear behavior appears, as is expected from the shape of the string frame metric in FIG. 4.3. The dashed line illustrates that the long-range part of calculated potential is almost linear.[12] We observe that the bulk reconstructed from the $\rho$ meson spectrum describes the quark confinement.

Subsequently let us investigate the nonlinear part. To this end, we subtract the linear part from $E(d)$ and fit the remaining, defined as $\tilde{E}(d)$, by three kinds of simple

[12]To evaluate the gradient of this part is interesting because it is interpreted as a QCD string tension in the context of the sting flux tube model of hadrons, but this is out of the scope of this paper due to the unknown constant $\alpha'$.

functions. The best-fit results of each function are shown in FIG.4.5 along with $\tilde{E}(d)$. We employ $1/d, 1/d^{\sigma}, \exp(\sigma d)$ as the model functions, among which the last one is found to be the best to approximate the nonlinear behavior.[13]

Regarding the nonlinear part of the generic quark potential at large $d$, it is known that the leading correction following the linear part is order $1/d$, which is referred to as the Lüscher term [35]. This behavior has been checked with the quark potential computed in lattice simulation [36]. [14] In contrast, our result does not show the dependence of $1/d$ as seen in FIG. 4.5. This is still fine because the Lüscher term is provided by a quantum fluctuation of the probe flux QCD string and thus of a fundamental string in the holographic perspective [39] while we treat the probe string with no fluctuation so far. In this sense Lüscher term should not appear in our study, and our result is consistent with QCD.

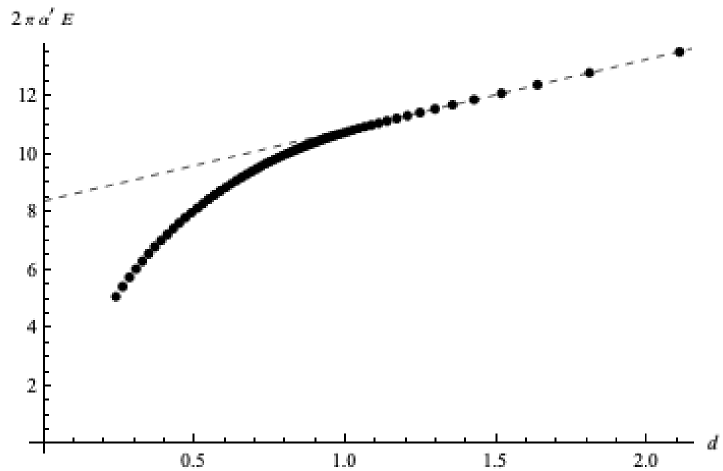


Figure 4.4: Quark-antiquark potential $2\pi\alpha' E(d)$ calculated with the string frame metric in FIG. 4.3. Horizontal axis $d$ is measured in the unit of the AdS radius $L = 0.51$[fm][15].

[13]The exponential suppression coincides with the result reported in the popular top-down models [34] where other behavior was also studied.

[14]Early results in the comparison between the lattice result and the AdS/QCD model approach without quantum fluctuation are found in [37, 38].

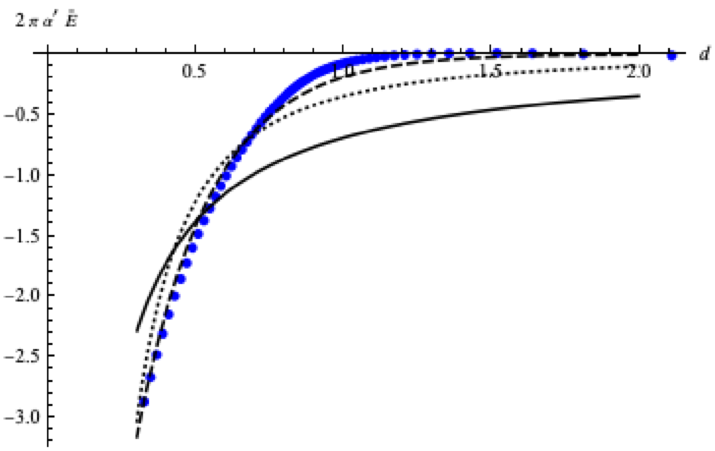


Figure 4.5: $E(d)$ is plotted with its linear contribution subtracted (blue points). We fit it by $\xi_1/d$ (solid line), $\xi_2/d^{\sigma_2}$ (dotted) and $\xi_3 \exp(\sigma_3 d)$ (dashed) where $\xi_i$ and $\sigma_i$ are fitting parameters.

# 5 Deriving dilaton potential in improved holographic QCD II

In this section, we study the non-zero temperature case to see whether this data-driven modeling of machine-learning holographic QCD works in more generic situations. We find the dilaton potential of the bulk action, for the metric found in [6]. This metric is holographically consistent with the lattice QCD data of chiral condensate as a function of the quark mass. The solver is the neural ordinary differential equations (neural ODE) [40], a machine learning technology suitable for continuous systems rather than discretized systems. The gravity equations at non-zero temperature has less symmetries: the metric has two independent components to be determined (on the other hand, the zero-temperature metric has only one component to be determined). Thus, the determination of the bulk action by its solution is even more nontrivial. We completely demonstrate that it is possible, and derive the dilaton potential in the bulk, only by using the explicit form of the metric solution.

With the obtained bulk action, we can compute the Wilson loop as a prediction of the holographic model. The model predicts that the string breaking distance at the temperature $T = 208$ [MeV] is $d_{\mathrm{W}}^{\mathrm{c}} \sim 0.5$ [fm]. This prediction turns out to be consistent with various lattice QCD simulation results, which shows a nontrivial consistency and the predictive power of the machine-learning holographic model and the AdS/DL correspondence.

The organization of this section is as follows. In section 5.1, we briefly review the results obtained in [6] for finding the metric from the chiral condensate data. We rerun the neural ODE with the metric ansatz dedicated to the improved holographic QCD. In section 5.2 we use the metric to derive the dilaton potential. We analyze the asymptotic behavior of the dilaton potential. In section 5.3 we calculate the holographic Wilson loop of the machine-learned model for our prediction and find that it agrees with various other lattice QCD results. Related to this section, Appendix A.6 is dedicated for the neural ODE training details, and Appendix 5.4 is for the symmetric property of the fields in our model.

## 5.1 New results for emergent metric in AdS/DL

The bulk geometry of the holographic QCD describing the dual of the chiral condensate was obtained numerically in [6] by the use of the machine learning. The scheme was based on the AdS/DL correspondence [5]. This was refined in [41] in which, instead of using deep neural networks composed of piles of layers, the neural ODE [40] was employed which enabled the use of continuous layers, *i.e.* continuous bulk geometries in the AdS/CFT.

In this section, we report new results which improve the bulk geometries previously obtained in [41]. The major improvement is about the following three respects.

The first improvement is about the spatial range of the bulk geometry. Originally in [41] the reconstructed geometry by the neural ODE was in the range $0.1 \leq \eta \leq 1$ in the unit $L = 1$ where $L$ is the AdS radius, and here we extend the range to the region $0.01 \leq \eta \leq 1$. With this, the region near the horizon of the black hole in the bulk geometry is better approximated, as the black hole horizon sits at $\eta = 0$.

The second improvement is about the prior knowledge about the metric function. The neural ODE uses a functional ansatz for the neural network weights which are bulk metric function $h(\eta)$ in our case. Here $h(\eta)$ is defined as, introducing a dilaton $\Phi$,

$$h(\eta) \equiv \partial_\eta \log\Big(\sqrt{f g^3 e^{-\Phi}}\Big), \tag{5.1}$$

in terms of a bulk metric in the string frame

$$ds^2_{\mathrm{sf}} = -f(\eta)dt^2 + d\eta^2 + g(\eta)ds^2_{\mathbb{R}^3}, \tag{5.2}$$

with the 3-D flat space metric $ds^2_{\mathbb{R}^3}$. The metric (5.2) is assumed to interpolate AdS vacuum in the limit of $\eta = \infty$ with the AdS radius $L$,

$$\lim_{\eta\to\infty} \partial_\eta \log f(\eta) = \lim_{\eta\to\infty} \partial_\eta \log g(\eta) = \frac{2}{L} \tag{5.3}$$

and the black hole (BH) horizon fixed at $\eta = 0$ as

$$\lim_{\eta\to 0} \eta\, \partial_\eta \log f(\eta) = 2, \quad \lim_{\eta\to 0} \partial_\eta \log g(\eta) = 0. \tag{5.4}$$

As for the machine learning applied to the emergent metric, we employ the following ansatz for $h(\eta)$,

$$h(\eta) = h^{\mathrm{nODE}}(\eta) \equiv \frac{1}{\eta} + b_1\eta + b_3\eta^3 + b_5\eta^5. \tag{5.5}$$

The first term is the singularity due to the black hole horizon, which is determined automatically for generic horizons with non-zero temperature. The remaining terms give our ansatz for the bulk geometry, where $b_1, b_3$ and $b_5$ are the coefficients which are trained in the neural ODE. Note that here we have only terms with odd powers in $\eta$, while in the work [41] all possible powers in the Taylor expansion were included. The reason of the current restriction of the powers is that in the Einstein dilaton system only

| $m_q$[GeV] | $\langle\bar{q}q\rangle[(\text{GeV})^3]$ |
|---|---|
| 0.00067 | 0.0063 |
| 0.0013 | 0.012 |
| 0.0027 | 0.021 |
| 0.0054 | 0.038 |
| 0.011 | 0.068 |
| 0.022 | 0.10 |

Table 5.1: Chiral condensate as a function of quark mass [42], at the temperature $T = 0.208$ [GeV], converted to physical units [6].

| Trial | $L$ [GeV$^{-1}$] | $\lambda$ | $b_1$ | $b_3$ | $b_5$ |
|---|---|---|---|---|---|
| #1 | 3.660 | 0.004868 | $-3.449$ | 6.517 | $-1.242$ |
| #2 | 3.613 | 0.005587 | $-3.317$ | 6.478 | $-1.547$ |

Table 5.2: Trained results by the neural ODE.

the odd powers are allowed since the system has a certain $\mathbb{Z}_2$ parity. See Appendix 5.4 for the derivation of the restriction.

The third improvement is on the regularization. We select the form of the regularization suitable for the Einstein-dilaton system, see Appendix A.6 for the details.

With these three improvements, we recapitulate the procedures provided in [41] to obtain the metric. Table 5.1 is the lattice QCD data which we use as the training data. It is the data of the chiral condensate $\langle\bar{q}q\rangle[(\text{GeV})^3]$ as a function of the quark mass $m_q$[GeV] at the temperature $T = 0.208$ GeV, obtained by the RBC-Bielefeld collaboration [42]. The network architecture and the holographic model are exactly the same as that of [41], except for the improvement described above. In Table 5.2 we list two successfully trained results of the neural ODE. The trained metric function is quite close to what was obtained previously in [41, 6]. Note that for each of these trials in Table 5.2 we slightly vary the value of the regularization coefficients, therefore the difference among the trials is not the statistical error.[15]

In the following, we are going to use the trained metric (5.5) with the coefficients given in Table 5.2, for the derivation of the dilaton potential in the dilaton-Einstein system in the holographic QCD.

[15]For the definition of the regularization and the details of the neural network architecture, see Appendix A.6.

## 5.2 Emergence of dilaton potential

In this section, we determine all the components of the metric and the dilaton potential from the metric combination $h(\eta)$ defined in (5.1) whose explicit form was provided by the lattice data of the chiral condensate by the neural ODE in the previous section.

We shall determine the metric components such that these boundary conditions are satisfied for the consistency of the AdS/CFT correspondence.

### 5.2.1 Einstein-Dilaton model

Continuing from the previous section, we consider the five-dimensional Einstein-dilaton model

$$S_5 = \frac{1}{2\kappa_5}\int d^5x\sqrt{-g}\left(R - \frac{4}{3}(\partial\Phi)^2 + V_D(\Phi)\right), \tag{5.6}$$

with an unknown dilaton potential $V_D(\Phi)$[16] which is assumed to be smooth. The metric (5.2) and the dilaton are supposed to be produced as a solution of this system. In the following, let us consider how to determine the explicit dilaton potential $V_D(\Phi)$ with which the equations of motion of (5.6) is solved with the emergent $h(\eta)$.

The introduced dilaton field $\Phi$ satisfies the boundary conditions

$$\lim_{\eta\to 0}\Phi = \Phi_0, \quad \lim_{\eta\to\infty}\Phi = \Phi_\infty \equiv 0, \tag{5.7}$$

with a certain positive-definite value $\Phi_0$. In addition, $\Phi(\eta)$ is expected to be a monotonically decreasing function,[17]

$$\partial_\eta\Phi(\eta) < 0 \quad \text{for } \eta > 0, \tag{5.8}$$

and thus, there is a one-to-one mapping between the coordinate $\eta$ and dilaton $\Phi$: $\eta \in \mathbb{R}_{\geq 0} \leftrightarrow \Phi = \Phi(\eta) \in (0, \Phi_0]$ as usually is in the AdS/CFT correspondence.

Let us derive the equations of motion of the system. Due to the existence of dilaton, we need to distinguish the metric in the string frame and that in the Einstein frame. We parameterize the metric in the Einstein frame as

$$ds^2_{\text{Ef}} = -f_{\text{Ef}}dt^2 + \rho(\eta)^2 d\eta^2 + g_{\text{Ef}}dx_m dx^m, \tag{5.9}$$

$$f_{\text{Ef}} = fe^{-\frac{4}{3}\Phi} = \exp\left(\frac{1}{2}(\psi(\eta) + 3\chi(\eta))\right), \tag{5.10}$$

$$g_{\text{Ef}} = ge^{-\frac{4}{3}\Phi} = \exp\left(\frac{1}{2}(\psi(\eta) - \chi(\eta))\right). \tag{5.11}$$

[16] Note that the sign of the potential is reversed from the normal one here so that $V_D$ will be positive almost everywhere. This follows the convention of previous studies.

[17] We guess that any oscillating $\Phi(\eta)$ background implies instability of the system against large fluctuations of $\Phi$ and must be prohibited.

Two metrics (5.2), (5.9) are related via a Weyl transformation, $ds^2_{\rm Ef} = e^{-\frac{4}{3}\Phi} ds^2_{\rm sf}$. Then we find that the equations of motion for $\psi$, $\chi$, $\Phi$ and $\rho$ result in, respectively,

$$0 = 2\partial_\eta v + v^2 + w^2 + \frac{4}{3}\partial_\eta \Phi\, v + \frac{16}{9}(\partial_\eta \Phi)^2 - \frac{4}{3} V_D e^{-\frac{4}{3}\Phi}, \tag{5.12}$$

$$0 = \partial_\eta w + vw + \frac{2}{3}\partial_\eta \Phi\, w, \tag{5.13}$$

$$0 = \partial_\eta^2 \Phi + v\, \partial_\eta \Phi + \frac{2}{3}(\partial_\eta \Phi)^2 + \frac{3}{8}\frac{\partial V_D}{\partial \Phi} e^{-\frac{4}{3}\Phi}, \tag{5.14}$$

$$0 = e^{\frac{4}{3}\Phi}\left(-\frac{3}{4}v^2 + \frac{3}{4}w^2 + \frac{4}{3}(\partial_\eta \Phi)^2\right) + V_D, \tag{5.15}$$

where we introduced $v \equiv \partial_\eta \psi, w \equiv \partial_\eta \chi$, and chose a gauge $\rho = e^{-\frac{2}{3}\Phi}$. The reason for the field redefinition (5.10) and (5.11) is that the resultant equations of motion are simpler and diagonalized.

We note here that the four equations of motion are not independent. In fact, one of them can be derived from the other three. Below, we briefly discuss the reason for that. Instead of introducing Eq.(5.9), let us write the metric in the Einstein frame as

$$ds^2_{\rm Ef} \;\; = \;\; -f_{\rm Ef} dt^2 + \rho^2 d\xi^2 + g_{\rm Ef} dx_m dx^m, \tag{5.16}$$

where an introduced coordinate $\xi$ is related to $\eta$ with a certain one-to-one mapping, satisfying

$$d\xi = \rho^{-1} e^{-\frac{2}{3}\Phi} d\eta. \tag{5.17}$$

By substituting metric (5.16) to anction (5.6) and omitting surface terms, we obtain the following reduced action per unit four-dimensional volume

$$S_{\rm rd} \;\; = \;\; \int d\xi\, e^{\psi} \left\{ -\frac{1}{\rho} K + \rho V_D \right\}, \tag{5.18}$$

$$K \;\; = \;\; -\frac{3}{4}(\partial_\xi \psi)^2 + \frac{3}{4}(\partial_\xi \chi)^2 + \frac{4}{3}(\partial_\xi \Phi)^2. \tag{5.19}$$

Here $\rho$ is regarded as an einbein of this one-dimensional model and e.o.m of $\rho$ gives

$$0 = \frac{\delta S_{\rm rd}}{\delta \rho} = \frac{1}{\rho^2} K + V_D, \tag{5.20}$$

which is usually regarded as a constraint. By taking this constraint into account, an arbitrary solution of e.o.ms of this reduced model automatically satisfies those for the original five-dimensional model.[18] General coordinate transformation invariance

[18] Thanks to symmetries which the ansatz posses, all components of the Einstein equation can be written by linear combinations of those for the reduced action as

$$\frac{\delta S_5}{\delta g_{tt}} \propto \frac{\delta S_{\rm rd}}{\delta f_{\rm Ef}}, \quad \frac{\delta S_5}{\delta g_{\eta\eta}} \propto \frac{1}{2\rho}\frac{\delta S_{\rm rd}}{\delta \rho}, \quad \frac{\delta S_5}{\delta g_{mn}} \propto \frac{\delta_{mn}}{3}\frac{\delta S_{\rm rd}}{\delta g_{\rm Ef}}. \tag{5.21}$$

guarantees the following identity

$$\rho\,\partial_\xi\left(\frac{\delta S_{\rm rd}}{\delta\rho}\right)=\sum_{X=\psi,\chi,\Phi}\partial_\xi X\frac{\delta S_{\rm rd}}{\delta X}. \tag{5.22}$$

Therefore, for nontrivial configurations, one of three equations for $\psi,\chi,\Phi$ is automatically satisfied if the others and the constraint are solved.

Let us obtain the consistent and independent set of equations of motion. By eliminating the potential $V_D$ from Eq.(5.12) using Eq.(5.15), we obtain a simpler equation

$$0=\partial_\eta v+w^2+\frac{2}{3}\partial_\eta\Phi v+\frac{16}{9}(\partial_\eta\Phi)^2. \tag{5.23}$$

We can choose Eqs.(5.15), (5.13) and (5.23) as independent equations, and if all of them are solved, Eq.(5.14) is automatically solved as is mentioned above.

In order to solve the three equations systematically, we massage the set of equations further. Since the potential $V_D$ appears only in Eq.(5.15) within those three equations, Eq.(5.15) can be regarded as an equation which implicitly determines the unknown $V_D$ if the one-to-one mapping (5.8) holds. Since $h(\eta)$ defined in Eq.(5.1) is calculated in terms of $v(\eta)$ as

$$h(\eta)=v(\eta)+\frac{5}{3}\partial_\eta\Phi(\eta), \tag{5.24}$$

using this $h(\eta)$, $\partial_\eta\Phi(\eta)$ in Eqs.(5.13) and (5.23) can be eliminated and we obtain

$$0=\partial_\eta v+w^2+\frac{6}{25}(v-h)\left(v-\frac{8}{3}h\right), \tag{5.25}$$

$$0=\partial_\eta w+\frac{1}{5}\left(3v+2h\right)w. \tag{5.26}$$

When a metric function $h(\eta)$ is given, therefore, these two equations are used to determine the two functions $v(\eta), w(\eta)$. The field $v$ and $w$ need to satisfy the boundary conditions

$$\lim_{\eta\to0}\eta v=1,\quad \lim_{\eta\to0}\eta w=1, \tag{5.27}$$

$$\lim_{\eta\to\infty}v=\frac{4}{L},\quad \lim_{\eta\to\infty}w=0. \tag{5.28}$$

Thus, in summary, our strategy to derive the dilaton potential is as follows. The input is the function $h(\eta)$ which the neural ODE determined explicitly. First, we solve Eqs.(5.25) and (5.26) under the boundary conditions (5.27) and (5.28), then second, we obtain $\Phi(\eta)$ by integrating Eq.(5.24), and finally we obtain the dilaton potential $V_D$ by using Eq.(5.15).

As a side remark, note that if we set $\Phi(\eta) = \Phi_0 = 0$, the system reduces to one for the pure Einstein gravity and the exact solution for $v, w$ is given by, with $V_D = 12/L^2$,

$$v(\eta) = v_{\mathrm{E}}(\eta) \equiv \frac{4}{L} \coth \frac{4\eta}{L}, \tag{5.29}$$

$$w(\eta) = w_{\mathrm{E}}(\eta) \equiv \frac{4}{L} \operatorname{csch} \frac{4\eta}{L}. \tag{5.30}$$

In this paper $\Phi(\eta)$ takes a non-trivial configuration with $\Phi_0 > 0$.

### 5.2.2 Asymptotics and extrapolation of $h(\eta)$

In section5.1, $h^{\mathrm{nODE}}(\eta)$ was numerically determined but it covers the limited region $0.01 < \eta < 1$ and it is technically hard to extend this region, whereas a solution of $v, w$ may critically depend on the boundary conditions (5.27) and (5.28). Therefore, we have to seriously consider an asymptotic behavior of $h(\eta)$ and need to extrapolate the trained $h(\eta)$ with using an appropriate extrapolation function. In this subsection, we study the asymptotic regions of the spacetime: $\eta \sim 0$ and $\eta \sim \infty$.

### 5.2.3 Near horizon behavior at $\eta \sim 0$

Focusing only on the mathematical aspects of this system of equations for $v, w$, the function $h$ can be arbitrarily imputed there, but as discussed bellow, some reasonable accompanying assumptions lead to several properties that the function must have.

At first, by assuming the smoothness of $V_D(\Phi)$ around the point $\Phi = \Phi_0$ corresponding to the horizon $\eta = 0$ we can consider (Laurent series) expansions of $v, w$ and $h$ around $\eta = 0$ and define $\mathbb{Z}_2$ parities of those functions. All of the equations and the boundary conditions allow us to set $v(\eta), w(\eta)$ and $\partial_\eta \Phi(\eta)$ to all odd functions, and in fact, it can be shown that they must be so. See Appendix.5.4. That is, they are expanded as

$$\begin{aligned} v(\eta) =& \frac{1}{\eta} + \sum_{n=1}^{\infty} a_n^{(v)} \eta^{2n-1}, \quad w(\eta) = \frac{1}{\eta} + \sum_{n=1}^{\infty} a_n^{(w)} \eta^{2n-1}, \\ \Phi(\eta) =& \Phi_0 + \sum_{n=1}^{\infty} a_n^{(\Phi)} \eta^{2n}, \end{aligned} \tag{5.31}$$

and especially, $h(\eta)$ must be expanded as

$$h(\eta) = \frac{1}{\eta} + \sum_{n=1}^{\infty} b_{2n-1} \eta^{2n-1}, \tag{5.32}$$

as we have already used in Eq.(5.5).[19] Using the equations of motion, their first terms are related with each other as

$$a_1^{(v)} = 2c_{\mathrm{h}} + \tilde{c}_{\mathrm{h}}, \quad a_1^{(w)} = -c_{\mathrm{h}} + \tilde{c}_{\mathrm{h}},$$
$$a_1^{(\Phi)} = -\frac{9}{4}\tilde{c}_{\mathrm{h}}, \quad b_1 = 2c_{\mathrm{h}} - \frac{13}{2}\tilde{c}_{\mathrm{h}}, \tag{5.34}$$

where $c_{\mathrm{h}}$ and $\tilde{c}_{\mathrm{h}}$ are defined as

$$c_{\mathrm{h}} = \frac{2}{9}V_D(\Phi_0)e^{-\frac{4}{3}\Phi_0},$$
$$\tilde{c}_{\mathrm{h}} = \frac{1}{24}\frac{\partial V_D}{\partial \Phi}(\Phi_0)e^{-\frac{4}{3}\Phi_0}. \tag{5.35}$$

This means that if the functional forms of $V_D(\Phi)$ had been given, the coefficients would have been controlled only by the initial value $\Phi_0$ without introducing any other free parameters. However, we are going backwards: we solve the equations of motion for the given $h(\eta)$ and derive $V_D$. In the following subsection, what we will do technically is to solve the Eqs.(5.25) and (5.26) by a numerical shooting with varying $c_{\mathrm{h}}$. Another parameter $\tilde{c}_{\mathrm{h}}$ will be determined automatically by the last equation in Eq.(5.34).

### 5.2.4 Asymptotic AdS behavior at $\eta \sim \infty$

Next, let us look at the asymptotic AdS region of the spacetime. The neural ODE provides $h(\eta)$ only in the region $\eta < L$, thus we need to find an appropriate extrapolation function of $h(\eta)$ for the region $\eta > L$. For this, we study the analytic behavior of the fields in the asymptotic AdS region.

The assumption of the AdS vacuum in the limit of $\eta = \infty$ requires that the potential $V_D$ behaves around the origin $\Phi = 0$ as

$$V_D(0) = \frac{12}{L^2}, \quad \frac{\partial V_D}{\partial \Phi}(0) = 0. \tag{5.36}$$

[19] If we expect the potential to behave as $V_D \sim \Lambda e^{2Q\Phi}\Phi^P$ for large $\Phi$ with certain constants $Q, P$ and $\Lambda$, and the value $\Phi_0$ is also sufficiently large like $\mathcal{O}(10)$ even in the finite temperature, then $b_1$ is also expected to be

$$b_1 \sim -\frac{13}{24}\left(Q - \frac{32}{39} + \frac{P}{2\Phi_0}\right)\Lambda e^{2(Q-\frac{2}{3})\Phi_0}\Phi_0^P. \tag{5.33}$$

According to [], they have been predicted $Q = 2/3, P = 1/2$ and thus, this prediction indicates $b_1 > 0$, whereas its magnitude is smaller than $\mathcal{O}(10)$ with using $\Lambda = \mathcal{O}(10)$. On the other hand, if $Q \sim 2\sqrt{2}/3$, $b_1$ should take a negative value of much larger magnitude. Thus, the sign of $b_1$ has a lot to do with our expectations.

Here, we just assume[20] that the dilaton mass $m_\Phi$ around the vacuum satisfies

$$m_\Phi^2 \equiv -\frac{3}{8}\frac{\partial^2 V_D}{\partial \Phi^2}(0) > 0. \tag{5.37}$$

Around this vacuum, $\Phi$ and $w$ behave as

$$\Phi \sim c_\Phi^+ \, e^{-p_+\eta}, \quad w \sim \frac{c_w}{L}\, e^{-4\frac{\eta}{L}}, \tag{5.38}$$

and then, $v$ behaves as

$$v \sim \frac{4}{L} - \frac{8c_\Phi^+}{3L} e^{-p_+\eta} + \frac{c_w^2}{8L} e^{-8\frac{\eta}{L}}, \tag{5.39}$$

with constants $c_\Phi^+, c_w$. Here $p_+$ is given by

$$p_\pm \equiv \frac{1}{L}\left(2 \pm \sqrt{4 + m_\Phi^2 L^2}\right) \in \mathbb{R}. \tag{5.40}$$

Therefore, $h(\eta)$ obtained in Eq.(5.24) must behave as

$$h(\eta) \sim h^{\mathrm{ex}}(\eta) \equiv \frac{4}{L}\left(1 - B_h e^{-p\eta}\right) \tag{5.41}$$

with certain constants[21] $B_h, p$. Under the assumption of $m_\Phi^2 \geq 0$, $p$ is given as $p = \min\{p_+, 8/L\}$ and takes a value in the narrow region[22]

$$\frac{4}{L} < p \leq \frac{8}{L}. \tag{5.44}$$

After these analytical observations, we find that it is natural to extrapolate the trained $h(\eta) = h^{\mathrm{nODE}}(\eta)$ in Eq.(5.5) to a region for large $\eta$ by using $h^{\mathrm{ex}}(\eta)$ given in

[20] Note that the BF bound $m_\Phi^2 \geq -4/L^2$ for the stability of the AdS vacuum is weaker than this condition. Intuitively, if $0 \geq m_\Phi^2 \geq -4/L^2$, then long-range interaction by dilaton distorts the asymptotic AdS spacetime to the extent that it becomes an obstacle for training $h(\eta)$.

[21] The coefficient $B_h$ controls the whole functional form of $h(\eta)$. In fact, when $h(\eta)$ has a valley in its profile, $B_h$ must be positive. This is realized when $m_\Phi^2$ is not so large,

$$B_h = \frac{8 + 5p_+L}{12} c_\Phi^+ > 0, \quad \text{for } 0 < m_\Phi^2 < \frac{32}{L^2}, \tag{5.42}$$

because the assumption (5.8) requires $c_\Phi^+ > 0$. On the other hand, for $m_\Phi^2 > 32/L^2$, $B_h$ is negative as $B_h = -c_w^2/32 < 0$ with $p = 8/L$.

[22] If we consider the case with $0 > m_\Phi^2 \geq -4/L^2$, $p$ is given by $p = p_-$ and thus satisfies

$$0 < p \leq \frac{2}{L}, \tag{5.43}$$

since $\Phi$ behaves as $\Phi \sim c_\Phi^- e^{-p_-\eta}$. In this case, there are technical difficulties to train the function $h(\eta)$ from the data in Table 5.1.

| Trial | $p$ | $B_h$ |
|---|---|---|
| #1 | 7.582 | 575.5 |
| #2 | 5.330 | 71.51 |

Table 5.3: The values of $(p, B_h)$ determined to be smoothly connected to the neural ODE results.

Eq.(5.41) as

$$h(\eta) = \begin{cases} h^{\mathrm{nODE}}(\eta) & \text{for } \eta < 1 \\ h^{\mathrm{ex}}(\eta) & \text{for } \eta \geq 1 \end{cases} \tag{5.45}$$

in the unit $L = 1$, where two parameters $p, B_h$ are set by requiring the smoothness of $h(\eta)$ at $\eta = 1$ as

$$h^{\mathrm{nODE}}(1) = h^{\mathrm{ex}}(1), \quad \partial_\eta h^{\mathrm{nODE}}(1) = \partial_\eta h^{\mathrm{ex}}(1). \tag{5.46}$$

Note that we have to check if $p$ satisfies $4 < p \leq 8$. In fact, many trained $h^{\mathrm{nODE}}(\eta)$ with poor initial conditions have violated this with deriving too large $p$ and been rejected. Therefore we need to include regularizations for the neural ODE training, see Appendix.A.6. Finally, with $h^{\mathrm{nODE}}(\eta)$ given in Table 5.2, we obtain reasonable data for $h^{\mathrm{ex}}(\eta)$. We list it in Table 5.3.

We show the profiles of $h(\eta)$ for trial #1 and trial #2 as thick solid lines in Fig.5.1. One can see that there appears a deep valley in its profile. On the other hand, in the Einstein gravity case, $h_{\mathrm{E}}$ is explicitly given as $h(\eta) = h_{\mathrm{E}}(\eta) \equiv v_{\mathrm{E}}(\eta)$ with $v_{\mathrm{E}}(\eta)$ in Eq.(5.29), and is also plotted in Fig.5.1 where there is no valley in this case. The resulting $h(\eta)$ with the neural ODE is, therefore, qualitatively different from that in the Einstein gravity case.

### 5.2.5 Deriving $V_D(\Phi)$ from $h(\eta)$

Here we are ready to calculate the unknown potential $V_D(\Phi)$ numerically from the trained $h(\eta)$ with the extrapolation (5.45). This needs a numerical integration of the equations of motion by the shooting method regarding the unknown coefficient $c_h$, as is explained below.

Let us solve Eqs.(5.25) and (5.26) with this given $h(\eta)$ to obtain $v(\eta), w(\eta)$ for $\eta \in [\eta_{\mathrm{ir}}, \eta_{\mathrm{uv}}]$ in the unit $L = 1$. To be more precise, we take $\eta_{\mathrm{ir}} = 10^{-5}$ as a near-horizon cut-off and $\eta_{\mathrm{uv}} = 5$ as the asymptotic AdS cut-off, and apply the shooting method by integrating the equations from $\eta = \eta_{\mathrm{ir}}$ to $\eta = \eta_{\mathrm{uv}}$. At $\eta = \eta_{\mathrm{ir}}$, according to Eq.(5.34),

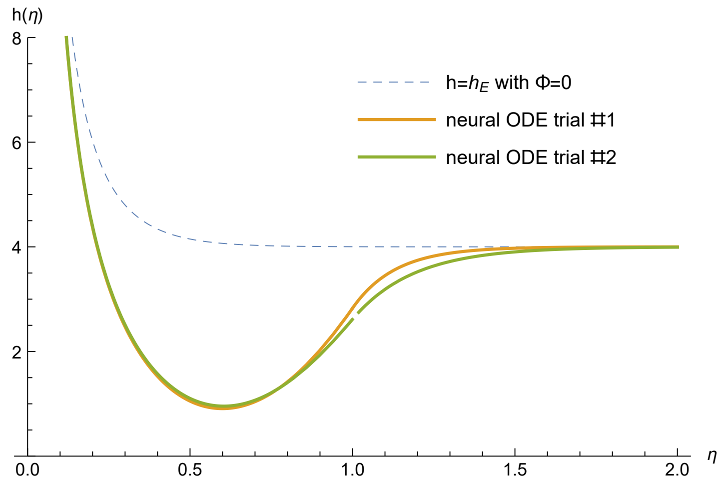


Figure 5.1: Fully extrapolated profiles of $h(\eta)$. Trial #1 and trial #2 are shown, in the unit $L = 1$. Differences between trial #1 and trial #2 become apparent in areas where the extrapolations have been used. The pure Einstein gravity case $h_E(\eta)$, shown with the dashed line, has no valley.

we take the initial values of $v, w$ as

$$v(\eta_{\rm ir}) = \frac{1}{\eta_{\rm ir}} + \frac{1}{13}\left(30c_{\rm h} - 2b_1\right)\eta_{\rm ir}, \tag{5.47}$$

$$w(\eta_{\rm ir}) = \frac{1}{\eta_{\rm ir}} - \frac{1}{13}\left(9c_{\rm h} + 2b_1\right)\eta_{\rm ir}, \tag{5.48}$$

where $b_1$ is a given parameter appearing in the expansion of $h(\eta)$ and $c_{\rm h}$ is regarded as a free parameter since its value is unknown. After integrating the differential equations, for large $\eta$ with $h \sim 4$, the value $v = h \sim 4$ turns out to be a saddle point since Eq.(5.25) reduces to be $\partial_\eta v \sim \frac{8}{5}(v-4)$, whereas $w \sim 0$ is automatically satisfied since $w = 0$ is an attractor as long as $3v + 2h > 0$. Therefore we must adjust the value of $c_{\rm h}$ precisely so that $v$ can satisfy

$$v(\eta_{\rm uv}) = h(\eta_{\rm uv}) \sim 4. \tag{5.49}$$

This is the numerical shooting. We start with some $\mathcal{O}(1)$ value of $c_h$ and start varying the value until the equation $v(\eta_{\rm uv}) = 4$ is attained. The procedure determines $v(\eta), w(\eta)$ numerically as plotted in Fig.5.2. These two $v, w$ are positive definite.[23]

[23] From Eqs.(5.23) and (5.13) and the boundary conditions (5.28), inequalities can be derived as

$$v > \frac{4}{L}e^{-\frac{2}{3}\Phi}, \quad w > 0. \tag{5.50}$$

The numerically searched value of $c_{\rm h}$ is

$$c_{\rm h} = \begin{cases} 3.373 & \text{(Trial \#1)} \\ 3.135 & \text{(Tiral \#2)}. \end{cases} \tag{5.51}$$

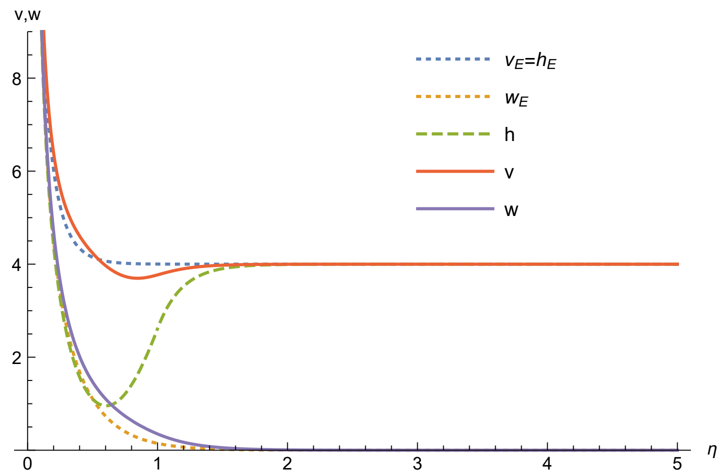


Figure 5.2: Figures of the functions $v, w$ determined by the integration, for trial #2.

After this procedure, thus, we can calculate the value of dilaton by using Eq.(5.24)
,

$$\Phi(\eta) \;=\; \frac{3}{5}\int_{\eta}^{\eta_{\rm uv}} d\eta'(v(\eta') - h(\eta')), \tag{5.52}$$

and the value of the potential at $\eta$,

$$V_D(\Phi(\eta)) = \qquad \frac{3}{4}e^{\frac{4}{3}\Phi}\left(v^2 - w^2 - \frac{16}{25}(v-h)^2\right), \tag{5.53}$$

by using Eq.(5.15). By combining them, finally we obtain a parametric representation of the potential $V_D(\Phi)$ for $\Phi \in [0, \Phi_0]$ as plotted in Fig.5.3. This concludes the complete determination of the bulk action by the QCD data of the chiral condensate, in the data-driven manner.

Let us study the obtained dilaton potential and discuss its physical implications. First, observe that, in Fig.5.3, each profile has a shallow valley.[24] The resulting potential for trial #2 is approximated by the following polynomial except in the vicinity

[24] This is an inevitable consequence of the requirement to be $m_\Phi^2 > 0$.

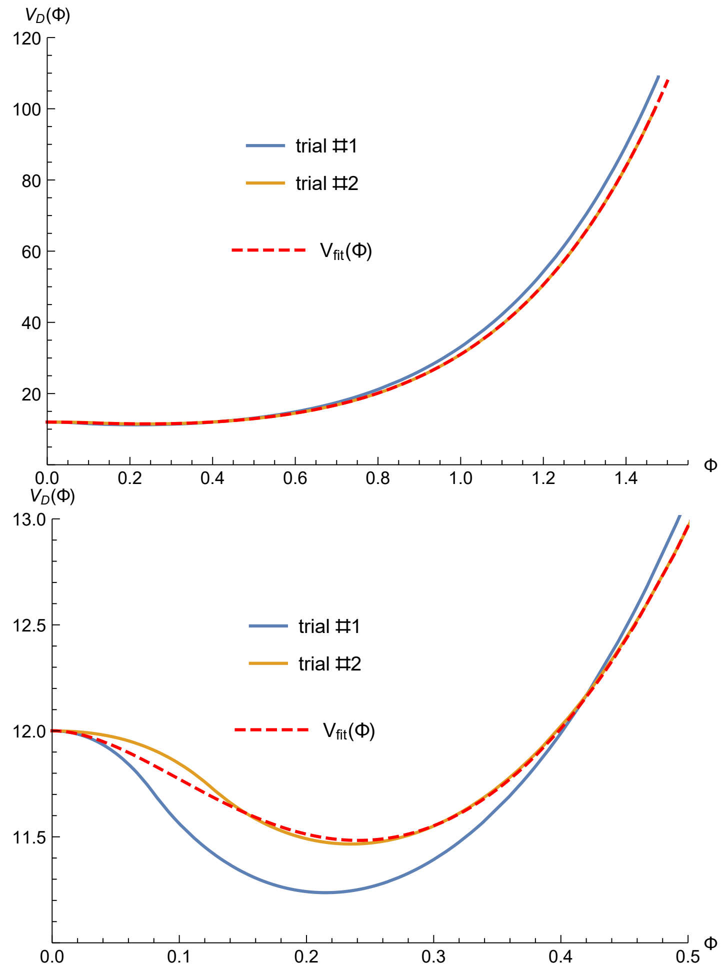


Figure 5.3: Profiles of $V_D(\Phi)$. The top panel shows the whole shape of the potential. The bottom panel is the one magnified for the vicinity of the origin.

of the origin of $\Phi$ corresponding to $\eta > 1$,

$$\begin{aligned} V_{\text{fit}}(\Phi) =& 12 - 38.5534\Phi^2 + 190.104\Phi^3 \\ & - 366.759\Phi^4 + 429.313\Phi^5 - 280.434\Phi^6 \\ & + 100.092\Phi^7 - 14.7622\Phi^8 \end{aligned} \tag{5.54}$$

as shown by the dashed line in Fig.5.3. Here, we imposed condition (5.36), but did not force the polynomial to fit the resulting data near the origin, as the influence of the manual extrapolation should be dominant there.

We look at the large $\Phi$ behavior of the potential in more details. The exponent of the resulting potential for a domain $[\Phi(0.5), \Phi(\eta_{\text{ir}})] \sim [0.85, 1.5]$, that is, for relatively large $\Phi$, can be approximated by exponential functions as,

$$\frac{d}{d\Phi} \log V_D(\Phi) \sim 1.20 + \frac{3.60}{\Phi} - \frac{2.45}{\Phi^2}. \tag{5.55}$$

as seen in Fig.5.4. The large $\Phi$ behavior of the dilaton potential in the IHQCD is closely

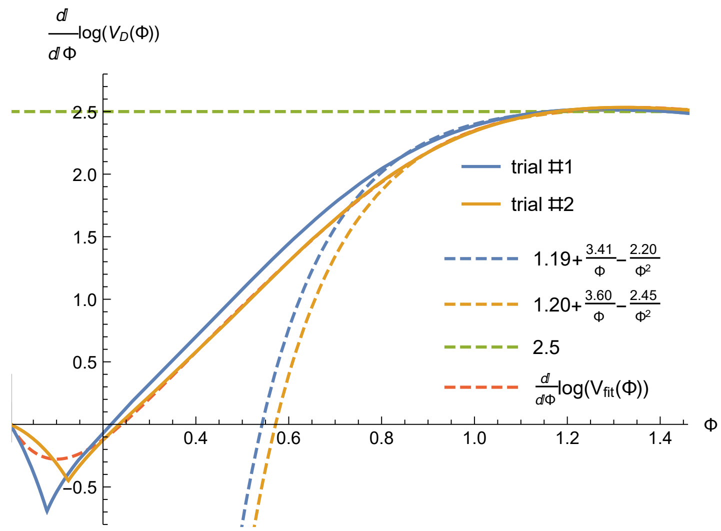


Figure 5.4: Profiles of $\frac{d}{d\Phi} \log V_D(\Phi)$, to extract the large $\Phi$ behavior of the dilaton potential $V_D$.

related to the hadron spectra. According to [26, 27], when $\Phi$ is sufficiently large, the Regge behavior of the glueball spectra leads to

$$\frac{d}{d\Phi} \log V_D(\Phi) \sim 2Q + \frac{P}{\Phi} \tag{5.56}$$

with $Q = 2/3$ and $P = 1/2$. We may say that our value $Q$ is close to this, and the order of our value $P$ is consistent with this.[25]

## 5.3 Prediction: Wilson Loop

Since we have obtained the hull bulk action, via the AdS/CFT dictionary we can compute various QCD quantities as a prediction of the holographic model. Here, as one of the basic predictions, we calculate the holographic Wilson loop, *i.e.* the quark-antiquark potential, and compare it with the lattice QCD results.

[25]Note that $\Phi_0 = \Phi(\eta_{\rm ir}) \sim 1.5$ is not large, so the precise comparison needs more study. For example, it would be interesting to derive the glueball spectra using our dilaton potential.

### 5.3.1 Temperature and metric

The calculation of the holographic Wilson loop needs the metric $f, g$ in the string frame, which are given by

$$f = e^{\frac{\psi+3\chi}{2}+\frac{4}{3}\Phi}, \quad g = e^{\frac{\psi-\chi}{2}+\frac{4}{3}\Phi}. \tag{5.57}$$

Note that in the previous section we have determined only $v = \partial_\eta \psi$ and $w = \partial_\eta \chi$, so to get the metric components, we need the integration:

$$\psi(\eta) = -\int_\eta^\infty d\eta' \left( v(\eta') - \frac{4}{L} \right) + \frac{4\eta}{L} + 4\delta_T, \tag{5.58}$$

$$\chi(\eta) = -\int_\eta^\infty d\eta' w(\eta'). \tag{5.59}$$

Here, when we make the integration, we are careful about the integration constant. The second equation (5.59) does not have the integration constant since we have the boundary condition $\chi(\infty) = 0$ which follows from the fact that the metric goes asymptotically to the pure AdS metric: $f/g \to 1$ as $\eta \to \infty$. The first equation (5.58) has a nontrivial integration constant $\delta_T$, which actually includes the temperature dependence of the metric. This constant needs to be determined such that the Hawking temperature $T$ appearing in the standard formula

$$f \sim (2\pi T \eta)^2 \quad \text{for} \quad \eta \sim 0 \tag{5.60}$$

is equal to the temperature of the QCD chiral condensate data which we used for the machine learning, $T = 208$[MeV]. Since the equation (5.60) deals with the coefficient of $\eta^2$ which is difficult to treat, let us introduce a function

$$F(\eta) \equiv \frac{\psi + 3\chi}{4} + \frac{2}{3}\Phi - \log\left(\tanh \frac{\eta}{L}\right) - \frac{\eta}{L}, \tag{5.61}$$

which behaves at the two asymptotics as non-zero constants,

$$F(\eta) \sim \begin{cases} \delta_T & \text{for } \eta \gg L \\ \log(2\pi T L) & \text{for } \eta \sim 0. \end{cases} \tag{5.62}$$

Then using the integral expression

$$\log\left(\tanh \frac{\eta}{L}\right) = -\int_\eta^\infty d\eta' \frac{2}{L} \,\text{csch}\, \frac{2\eta'}{L}, \tag{5.63}$$

we find

$$F(\eta) = \delta_T + \frac{2}{3}\Phi - \int_\eta^\infty d\eta' \left( \frac{v+3w}{4} - \frac{2}{L} \,\text{csch}\, \frac{2\eta'}{L} - \frac{1}{L} \right). \tag{5.64}$$

| Trial | $TL$ | $\Phi_0$ | $\delta_T$ | $d^{\rm c}_{\rm W}$[fm] | $T'_{\rm W}$[GeV$^2$] |
|---|---|---|---|---|---|
| #1 | 0.761 | 1.4782 | -0.216 | 0.543 | 0.32 |
| #2 | 0.751 | 1.4718 | -0.231 | 0.527 | 0.35 |

Table 5.4: Various resultant data.

Therefore, using the expression for $F(0) = \log(2\pi TL)$, we need to determine the integration constant $\delta_T$ as

$$\delta_T = \delta_{\rm ref} + \log(2\pi TL), \tag{5.65}$$

$$\delta_{\rm ref} \equiv \int_0^\infty d\eta \left( \frac{v+3w}{4} - \frac{2}{L} \operatorname{csch} \frac{2\eta}{L} - \frac{1}{L} \right) - \frac{2}{3}\Phi_0. \tag{5.66}$$

Using this formula, we can completely determine the metric components. Note that in reality we need to replace the integration region $(0, \infty)$ by $(\eta_{\rm ir}, \eta_{\rm uv})$ for our numerical purpose. The resulting data are summarized in Table 5.4.

In Fig.5.5, we plot profiles of $f, g$ for tiral #2 with taking $\delta_T = 0$ for simplicity, comparing them with those, $f = f_{\rm E}, g = g_{\rm E}$ calculated in the pure Einstein gravity case.

Note that in this dissertation we have assumed $m_\Phi^2 > 0$ which means $\Phi = 0$ is a top of a mountain in a sign-flipped potential. With this assumption, the dilaton profile is determined uniquely, so there will not be any temperature dependence. Basically this is because the profile of the dilaton and the initial value $\Phi_0$ are uniquely fixed such that the radial "motion" of the dilaton, which starts at $\Phi_0$ at "time" $\eta = 0$, has to stop at the top of the sign-flipped dilaton potential hill at " time" $\eta = \infty$. Then the solutions of $v(\eta), w(\eta), \Phi(\eta)$ are uniquely determined by giving an initial value $\Phi_0$ (see Eq. (5.34)), and thus the chiral condensate does not depend on the temperature. Note that the explicit temperature dependence in the metric appears only as a common overall coefficient $e^{2\delta_T}$ of $f, g$, as

$$(f, g) = (f, g)\Big|_{\delta_T=0} e^{2\delta_T} = (f, g)\Big|_{T=T_{\rm ref}} \times \left(\frac{T}{T_{\rm ref}}\right)^2, \tag{5.67}$$

with $T_{\rm ref} \equiv e^{-\delta_{\rm ref}}/2\pi L$. This overall factor is just the integration constant and does not appear in the expression of $h(\eta)$ which determines the chiral condensate. In this dissertation we have assumed $m_\Phi^2 > 0$, otherwise the strategy we have taken here does not work well technically. On the other hand, if we have adopted the case $m_\Phi^2 \leq 0$, $\Phi_0$ could to be a continuous moduli of the solution and the temperature dependence can be encoded in $\Phi_0$.

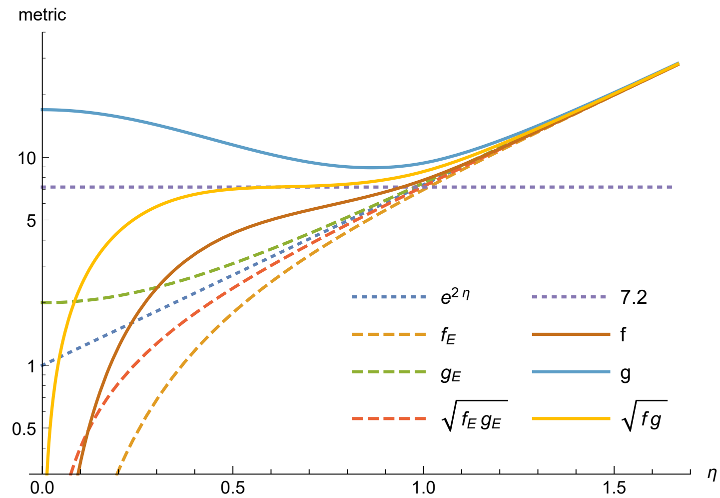


Figure 5.5: Log plot for the metric components $f$ and $g$ for trial #2, and their comparison with the pure Einstein gravity case $f_{\mathrm{E}}$ and $g_{\mathrm{E}}$. We took $\delta_T = 0, L = 1$ for simplicity.

### 5.3.2 Holographic Wilson loop

Let us place a quark and an antiquark on the AdS boundary, keeping the quark-antiquark separation distance $d_{\mathrm{W}}$, and consider a string hanging between them, of which the midpoint at $\eta = \eta_0$ is the deepest point of the string in the radial $\eta$ direction. According to [32, 33], the distance $d_{\mathrm{W}}$ is given in terms of $\eta_0$ as

$$d_{\mathrm{W}} = 2\int_{\eta_0}^{\infty} \frac{d\eta}{\sqrt{g(\eta)}} \sqrt{\frac{f(\eta_0)g(\eta_0)}{f(\eta)g(\eta) - f(\eta_0)g(\eta_0)}}, \tag{5.68}$$

which is plotted in Fig.5.6, using the training results #1 and #2.

The quark-antiquark potential $V_{\mathrm{W}}$ is calculated as

$$\begin{aligned} 2\pi\alpha' V_{\mathrm{W}} &= 2\int_{\eta_0}^{\infty} d\eta \sqrt{f(\eta)} \left( \sqrt{\frac{f(\eta)g(\eta)}{f(\eta)g(\eta) - f(\eta_0)g(\eta_0)}} - 1 \right) \\ &\quad -2\int_0^{\eta_0} d\eta \sqrt{f(\eta)}, \end{aligned} \tag{5.69}$$

where the infinite energy of parallel two straight strings hanging from the AdS boundary to the endpoint at the horizon has been subtracted from the potential to make this expression finite. Since the string configuration is determined such that the free energy of the string is minimized, the connected string with $V_{\mathrm{W}} > 0$ is not realized. If $V_{\mathrm{W}} > 0$, the configuration of the two parallel straight strings is realized. The latter means the Debye screening of the quarks.

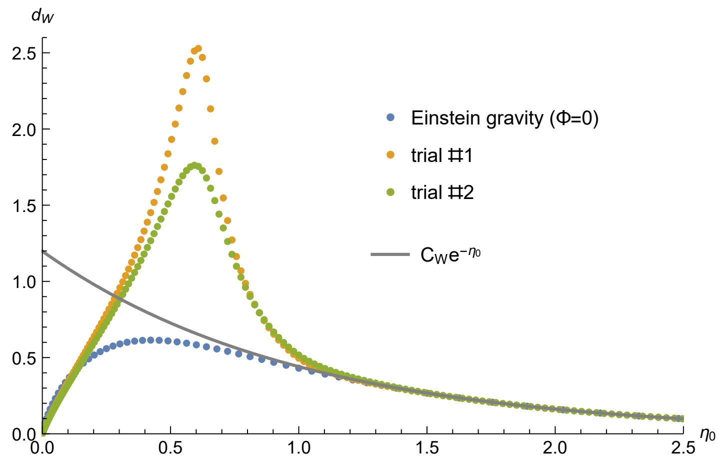


Figure 5.6: Profiles of $d_\mathrm{W}(\eta_0)$ with $L = 1$. Here $\delta_T = 0$ is formally taken for simplicity.

By combining the above two, we obtain a parametric representation of the function $V_\mathrm{W}(d_\mathrm{W})$ as is plotted in Fig.5.7. The multivalued potential stems from the existence

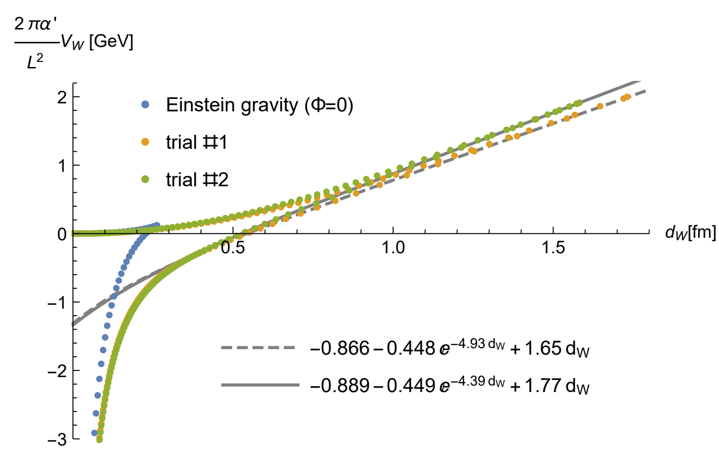


Figure 5.7: Profiles of $V_\mathrm{W}(d_\mathrm{W})$ in the Physical units.

of two solutions for $d_\mathrm{W}(\eta_0)$ in (5.68), see Fig.5.6. The upper branch is never realized, so one needs to look at only the lower branch in Fig.5.7. In addition, there is another configuration which is just a set of the straight parallel strings, giving $V_\mathrm{W} = 0$. Thus, in Fig.5.7, once the lower branch goes above the $d_\mathrm{W}$ axis, it is not realized and replaced by the line $V_\mathrm{W} = 0$.

These $d_\mathrm{W}$ and $V_\mathrm{W}$ in the physical unit are obtained by the following formulas

$$d_\mathrm{W} = d_\mathrm{W}\Big|_{L=1,\delta_T=0} \times \frac{e^{-\delta_\mathrm{ref}}}{2\pi T}, \tag{5.70}$$

$$\frac{2\pi\alpha'}{L^2} V_\mathrm{W} = 2\pi\alpha' V_\mathrm{W}\Big|_{L=1,\delta_T=0} \times 2\pi T e^{\delta_\mathrm{ref}}, \tag{5.71}$$

and information of $e^{\delta_T} = 2\pi T L e^{\delta_{\rm ref}}$ is easily restored.[26]

Let us look at the short-distance and long-distance behavior of the obtained quark-antiquark potential. First, as for the short-distance behavior at small $d_{\rm W}$ which corresponds to $\eta_0 \gg L$, we find

$$\frac{2\pi\alpha'}{L^2} V_{\rm W} = -\frac{C_{\rm W}^2}{d_{\rm W}} + \text{const.}, \tag{5.72}$$

where we have used

$$d_{\rm W} = \frac{e^{-\delta_{\rm ref}}}{2\pi T} \times C_W e^{-\frac{\eta_0}{L}}, \quad C_{\rm W} \equiv \frac{(2\pi)^{\frac{3}{2}}}{\Gamma(\frac{1}{4})^2}. \tag{5.73}$$

This $1/d_{\rm W}$ behavior is typical of conformal field theories, reflecting the fact that the string is in the pure AdS geometry. In fact, one can check that the quark potential is almost identical to that in the case of the pure Einstein gravity, see Fig. 5.7 and in particular the gray solid line in Fig.5.6. Note that the dimensionless coefficient $2\pi\alpha' L^{-2}$ is not the parameter of the model, so the overall normalization of the quark-antiquark potential cannot be predicted in this model.

The long-distance behavior of the quark-antiquark potential differs significantly from the case of Einstein gravity. In fact, ours possesses the confining linear potential,[27]

$$V_{\rm W} \sim T_{\rm W}(d_{\rm W} - d_{\rm W}^{\rm c}) \tag{5.74}$$

with constants $T_{\rm W}$ and $d_{\rm W}^{\rm c}$, as seen in Fig.5.7 and Fig.5.8. Therefore, the system develops the quark confinement. For trial#2, the string breaking scale $d_{\rm W}^{\rm c}$ determined[28] as an intersection with $V_{\rm W} = 0$, is

$$d_{\rm W}^{\rm c} = 0.587 \times \frac{e^{-\delta_{\rm ref}}}{2\pi T} = 2.67[\text{GeV}^{-1}] = 0.527[\text{fm}]. \tag{5.76}$$

This breaking distance is the physical prediction of the model.

Comparing Fig.5.5 and Fig.5.6, we find that this appearance of the linear potential is due to the existence of the plateau of the metric $\sqrt{fg}$ in Fig.5.5. Such a plateau does

[26]For instance, $\delta_{\rm ref} = -\log(2\sqrt{2})$ in the Einstein gravity case with $\Phi_0 = 0$.

[27]The subleading term is theoretically proven to dump exponentially. See section 3.3 in [34] for the proof.

[28]We observe that the tension $T_{\rm W}$ is

$$\begin{aligned} T'_{\rm W} \equiv \frac{2\pi\alpha'}{L^2} T_{\rm W} &\sim 7.2 \times (2\pi T e^{\delta_{\rm ref}})^2 \\ &\sim 0.35\,[\text{GeV}^2] = 1.8\,[\text{GeV}\cdot\text{fm}^{-1}]. \end{aligned} \tag{5.75}$$

Note that this is not the physical quantity as one needs the prefactor $2\pi\alpha'/L^2$ to compare it with the actual string tension in QCD.

not appear in that for the Einstein gravity case. Note that Eq.(5.68) and Eq.(5.69) are defined for $\eta_0$ so that $f(\eta)g(\eta)$ is a monotonically increasing function for all $\eta > \eta_0$ and the plateau immediately causes large value of $d_{\rm W}$ and $V_{\rm W}$. We can extract this large contribution from $V_{\rm W}$ using that in $d_{\rm W}$ by rewriting Eq.(5.69) as,

$$\begin{aligned} 2\pi\alpha' V_{\rm W} &= \sqrt{f(\eta_0)g(\eta_0)}\, d_{\rm W} \\ &\quad - 2\int_{\eta_0}^{\infty} d\eta \left(\sqrt{f(\eta)} - \sqrt{f(\eta) - \frac{f(\eta_0)g(\eta_0)}{g(\eta)}}\right) \\ &\quad - 2\int_0^{\eta_0} d\eta \sqrt{f(\eta)}. \end{aligned} \tag{5.77}$$

In this formula, only values of $V_{\rm W}$ and $d_{\rm W}$ drastically changes in the plateau and as a result we observe an almost linear potential there. We can read the tension $T_{\rm W}$ from this expression as

$$T'_{\rm W} = \frac{2\pi\alpha'}{L^2} T_{\rm W} \sim \frac{\sqrt{f(\eta_0)g(\eta_0)}}{L^2}, \tag{5.78}$$

which take an almost fixed value for $\eta_0$ in the plateau. In fact, we find that this formula is consistent with Eq.(5.75) and Fig.5.5.

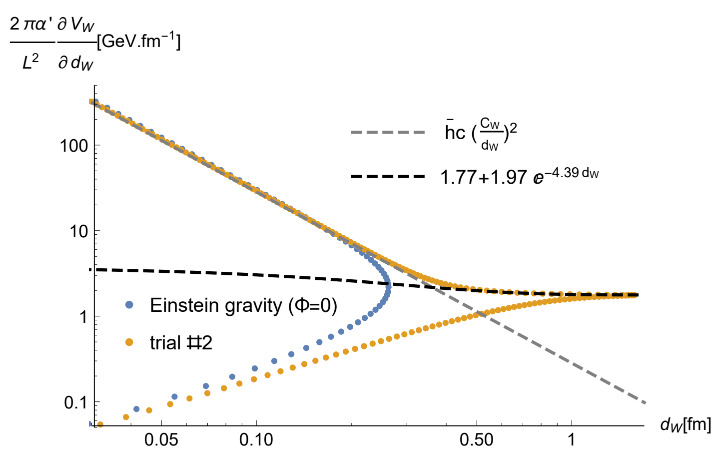


Figure 5.8: Log-log plot of $\frac{\partial V_{\rm W}}{\partial d_{\rm W}}(d_{\rm W})$ for trial #2 in the physical units.

Finally, in Fig.5.9 we compare our results with those of the lattice calculation [43], adjusting the origin and the scale of the vertical axis. The lattice data shows that the string breaking distance at $T \sim 200$ [MeV] is estimated as $d \sim 0.5$ [fm], which is in good agreement with our prediction $d_{\rm W}^{\rm c}$ given in (5.76). This agreement ensures the validity of the present model of the emergent dilaton potential.

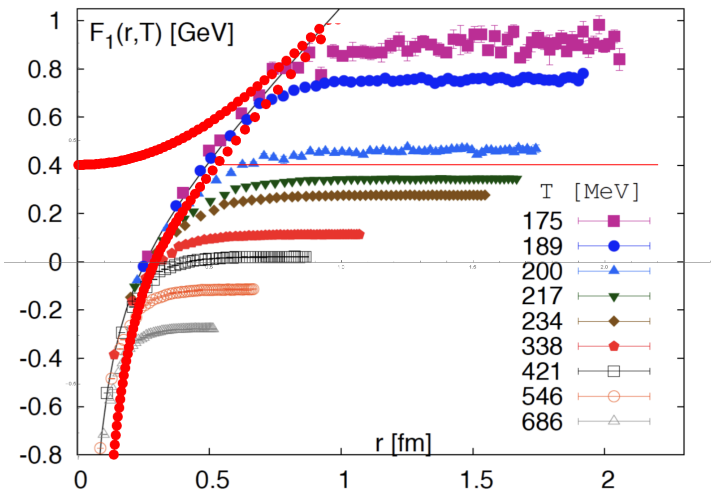


Figure 5.9: Comparison between the lattice data [43] (black and grey symbols) and our result for trial #2 (red dots and a red straight line) for the quark antiquark potential. The vertical axis is the potential, and the horizontal axis is the quark separation. The realized holographic potential is the lowest one among all the red dots and the red line at each value of the quark distance. To plot our result, we choose the value of $\alpha'$ such that the long distance behavior of our model fits that of the lattice data, to find that our fitting value is $L^2/2\pi\alpha' = 0.7$. In addition, since our model is for $T = 208$ [MeV], we set the zero of our potential as 0.4 [GeV] in the lattice data plot, which is the red line.

## 5.4 $\mathbb{Z}_2$ parity of functions

Even if the dilaton potential is unknown, an assumption that the potential is smooth leads to a certain $\mathbb{Z}_2$ parity in the solution of $v, w$ and $\Phi$ as the followings. Let us consider power series expansions of $v, w$ and $\Phi$ around $\eta = 0$,

$$\begin{aligned} v(\eta) &= v_{\text{odd}}(\eta) + \alpha_v \eta^n + \cdots , \\ w(\eta) &= w_{\text{odd}}(\eta) + \alpha_w \eta^{n'} + \cdots , \\ \Phi(\eta) &= \Phi_{\text{even}}(\eta) + \alpha_\Phi \eta^{n''+1} + \cdots , \end{aligned} \tag{5.79}$$

where $v_{\text{odd}}(\eta), w_{\text{odd}}(\eta)$ are odd functions with respect to $\eta$ and $\Phi_{\text{even}}(\eta)$ is even, and the rest of terms in the r.h.s are assumed to be not so, and $n, n', n'' \notin 2\mathbb{Z}+1$ are assumed to give the smallest powers within them, satisfying $n, n', n'' > -1$. By substituting these to the equations (5.12),(5.13) and (5.14) and taking an expansion around $\eta = 0$, we find that contributions coming from only $v_{\text{odd}}, w_{\text{odd}}$ and $\Phi_{\text{even}}$ give expansions of even powers. And thus focusing on the lowest order terms in the equations such that their order are not even, those contributions must give the linearized equations for the terms $\alpha_v\eta^n, \alpha_w\eta^{n'}$ and $\alpha_\Phi\eta^{n''+1}$ that are independent of the other contributions as,

$$0 =2(n{+}1)\alpha_v\eta^{n-1} + 2\alpha_w\eta^{n'-1} + \frac{4}{3}(n''{+}1)\alpha_\Phi\eta^{n''-1} + \cdots \tag{5.80}$$

$$0 =(n'{+}1)\alpha_w\eta^{n'-1} + \alpha_v\eta^{n-1} + \frac{2}{3}(n''{+}1)\alpha_\Phi\eta^{n''-1} + \cdots \tag{5.81}$$

$$0 =(n'' + 1)^2\alpha_\Phi\eta^{n''-1} + 2a_1^{(\Phi)}\alpha_v\eta^{n+1} + \cdots \tag{5.82}$$

with using the leading terms of $v_{\text{odd}}, w_{\text{odd}}, \Phi_{\text{even}}$ as background fields,

$$v_{\text{odd}}(\eta) \sim \frac{1}{\eta}, \quad w_{\text{odd}}(\eta) \sim \frac{1}{\eta}, \quad \Phi_{\text{even}}(\eta) \sim \Phi_0 + a_1^{(\Phi)}\eta^2. \tag{5.83}$$

If $\{\alpha_v, \alpha_w, \alpha_\Phi\}$ are assumed to be non-trivial, the first two equations requires $n = n' = n''$ and $\alpha_v, \alpha_w \propto \alpha_\Phi$, whereas the last equation requires that $\alpha_\Phi$ vanishes and that is, $\alpha_v = \alpha_w = \alpha_\Phi = 0$. This inconsistency shows that $v(\eta), w(\eta)$ must be odd functions and $\Phi(\eta)$ are even. That is, $f, g$ and $\Phi$ have formally the following $\mathbb{Z}_2$ properties,

$$f(-\eta) = f(\eta), \quad g(-\eta) = g(\eta), \quad \Phi(-\eta) = \Phi(\eta), \tag{5.84}$$

although we do not consider the inside of the BH horizon for $\eta < 0$. Especially, $h(\eta)$ must be an odd function

$$h(-\eta) = -h(\eta). \tag{5.85}$$

# 6 Conclusion and discussion

To conclude my dissertation, I would like to summarize our results and discuss further research.

In section 3, we have proposed a deep learning architecture to discover an AdS/QCD model from a given experimental data of meson mass spectra. The neural network depth direction is identified with the emergent radial direction $z$ of the 5-dimensional model. The model is a soft-wall model based on Ref. [9], with the unknown metric function $A(z)$ of the curved geometry and the unknown dilaton profile $\Phi(z)$. We have identified those profiles with weights of the deep neural network (FIG. 3.2). By the supervised training with the lowest and the second lowest $\rho$ and $a_2$ meson mass values as the training data, our machine has found optimized profiles of the geometry $A(z)$ and the dilaton $\Phi(z)$ (FIGs. 3.6 and 3.7). Therefore, the deep learning, based on the concept of AdS/DL [5, 6], can derive an effective AdS/QCD model from QCD experimental data.

With the emergent geometry and the dilaton profile, we have calculated the excited meson masses. This prediction has turned out to be reasonable, although it should not be taken seriously, as the architecture has various regularization and discretization errors. Nevertheless, the training to obtain the emergent geometry is worthwhile in a larger perspective. This framework may open a whole scheme of determining a better holographic model by a vast amount of data of QCD. As we have emphasized in section 1, QFT has an infinite number of data, which are spectra and scattering amplitudes, equivalent to $n$-point correlators of an infinite kinds of gauge invariant operators. Finding better holographic models is equivalent to the feature extraction of QCD, which may help revealing the hidden mechanism of how the AdS/CFT correspondence works.

Related to that, the similarity between the holographic dictionary and the deep neural network architecture may have some physical origin, and such a standpoint may provide a new way to investigate two subjects which appear distantly related: quantum gravity and data science. In the growing subject (see Ref. [44] for a recent summary of data science application to string theory), the idea of equating a holographic spacetime with neural network [5, 11, 6, 45, 10, 46, 47] may be intertwined with machine learning string landscapes initiated by Refs. [48, 49, 50, 51]. Discovering a complete gravity dual of QCD is a challenging problem, and various data-scientific methods applied to string theory may help for it.

In section 4 we have derived a new dilaton potential for IHQCD based on the gravitational duals machine-learned from the meson spectrum. The Einstein equations (4.6) are for the zero-temperature metric (4.5) and they include the dilaton potential $V(\Phi)$ to be determined. We have solved them by using the information of the machine-learned

$B'(z)$ obtained in [15] as a constraint on the equations then have determined the explicit form of $V(\Phi)$. Its analytic form is well-fit by a cosh function, while interestingly the cosh form is the potential used to reproduce the equation of state of QCD in [29]. Subsequently we have shown that the dilaton potential satisfies the asymptotic condition (4.4) with $(P, Q) = (1/2, 2/3)$ which is of the standard functional form for dilaton potentials employed in IHQCD. This asymptotic condition was determined phenomenologically for the glueball spectrum [26, 27], so it is surprising that the potential derived from the vector meson spectrum has turned out to satisfy the condition. Thus, as a sequence of processes, we have been able to construct a reasonable IHQCD model in a data-driven way.

Here we may make a comment on the fitting scheme of the obtained values of $(P, Q)$ in the derived dilaton potential. We have found that $P$ and $Q$ depend on $\Phi_c$ despite the trivial dependence as shown in (4.10). This happens because our fitting procedure only see a restricted region in $z$. The fit model (4.4) includes powers in $\Phi$. Then when the region of $\Phi$ for fit shifts by changing $\Phi_c$, the best fit parameters except for the overall constant also vary. This is a systematic issue to be improved and would be resolved if the bulk gravity can be more precisely reconstructed beyond $z = 4$. We may leave this as a future study.

Following the derivation of the IHQCD model, we have calculated the Wilson loop, a QCD quantity, as a concrete prediction of the holographic model. In this model, the metric has a structure with a valley in the bulk, where the probe string is expected to be stuck. The conventional calculation of the holographic Wilson loop has led to the quark-antiquark potential linear in the long-range region. For the nonlinear part of the potential, we have found that it is approximated by an exponential function. The origin of this behavior needs further study, but one explanation is by [52] in which it is shown that the leading nonlinearity of the holographic Wilson loop faster than $1/d$ always results in the valley, as is consistent with our emergent bulk metric in FIG. 4.3.

In this dissertation, we have treated only the Wilson loop as an observable of the boundary theory, but IHQCD can make predictions for various thermodynamic quantities once the dilaton potential is given. Thus, by comparing our model with lattice QCD calculations, we may be able to find a better agreement on the thermodynamic quantities than the existing models. We also have the advantage of being able to solve the equations again to derive a holographic model at finite temperature and calculate hydrodynamic observables describing the QGP phase. Furthermore, if a large number of various kinds of QCD data can derive a consistent dilaton potential, it leads to a construction of IHQCD models that describe QCD at various energy scales simultaneously. We will describe some models using different training QCD data in our future work [17], and hope that the combination of the holographic machine learning of quantum field theory data [11, 5, 6, 47, 10, 46, 53, 15, 41, 54] and further improvement of holographic QCD models will lift the final vail of "the gravity dual of QCD."

In section5 we have derived the dilaton potential (Fig. 5.3) in improved holographic QCD, from the lattice data of the chiral condensate as a function of the quark mass. First, we have improved the neural ODE provided in [41] for obtaining the bulk metric from the chiral condensate data. Then requiring that the emergent machine-learned metric is a solution of the bulk equations of motion of an Einstein-dilaton system, we have derived the dilaton potential uniquely. This completes the bulk reconstruction program.

The result of the neural ODE fixes only a certain combination of the metric components. However, requiring that they solve the equations of motion, we can constrain the dilaton potential in the bulk action and in fact can derive it. This determines all the metric component and the dilaton profile uniquely, at the same time. We have used the determined metric to calculate a holographic Wilson loop, and have obtained a prediction of the QCD-string breaking distance $d \sim 0.5$ [fm] at our temperature value $T = 208$ [MeV] (see (5.76)). This value is almost identical to what is known in lattice simulations (see Fig. 5.9).

We should confess that it was unexpected that the string breaking distance took the right value in our model, because the confinement and Debye screening of the quarks is not directly related to the behavior of the chiral condensate in QCD. In fact, in the previous estimate of the string breaking distance by the machine-learned metric [6], the estimated value is quite different from our value. There are two reasons for that. First, in [6] a guess for a certain component of the metric was used, while in our present work we have derived all the components of the metric by requiring that they should be derived from a single Einstein-dilaton system. Another reason is that we have improved the machine learning to refine the metric. So we conclude that the guess of the metric component in [6] was too naive, and once the bulk system is specified the prediction of the string breaking distance goes quite well.

Let us discuss a subtle and remaining issue of the model. In this work we considered only the data at $T = 208$ [MeV] and in the future work it is desirable to include all lattice data at various values of the temperature, to find a unique and consistent bulk action from which all the data is reproduced. Unfortunately, this appears to be difficult, as follows. If the dilaton potential $V_D$ does not explicitly have a temperature dependence, we may calculate $h(\eta)$ from the Einstein-dilaton system with the potential $V_D(\Phi)$, and then we will find that $h(\eta)$ has no temperature dependence at all. This contradicts the temperature dependence of the chiral condensate. Therefore, to find the consistent model for any temperature, we may need to loosen our assumptions used in this dissertation (such as $m_\Phi^2 > 0$), or we may need to consider more general bulk action with more terms. Other possibility would be to take into account the back reaction of the probe scalar field for the chiral condensate. These kinds of the generalized models deserve a detailed study.

At this stage, we have the dilaton potential obtained by independent procedure; derived from the lattice data of the chiral condensate in section 4 and the one obtained in section 5 with the data of the hadron spectra. They are expected to be consistent with each other. Let us make a brief comparison between these two dilaton potential. In fact, our dilaton potential is defined in the range of $0 \leq \Phi \leq 1.5$ while the dilaton potential in [16] is in $0 \leq \Phi \leq \mathcal{O}(20)$. The latter is insensitive to the detailed region near the origin. So, naively we can combine these two dilaton potentials to form a consistent single dilaton potential. This unified Einstein-dilaton system can recover both of the chiral condensate at the finite temperature and the $\rho$-meson spectra at zero-temperature. This is a qualitative statement, and still needs a detailed confirmation. For example, our obtained AdS radius $L \sim 3.6$ [GeV$^{-1}$] $= 0.71$ [fm] at $T = 0.208$ [GeV] is slightly different from the value $L \sim 0.51$ [fm] at $T = 0$ obtained in [16].

Since the data-driven holographic modeling is now possible as we have demonstrated in this dissertation and in [16], we would be ready to explore a unified holographic QCD model which reproduces all the physical observables of QCD. For this task, we need to compare various inversely-solved holographic models, as we have briefly tried above. Since QCD has infinite amount of data, the unification may need more machinery of deep learning.

Once a unified holographic QCD model is constructed, the most interesting direction is to investigate how we obtained the unified model from the string theory. The unified model is a junction of top-down approach and bottom-up approach. The data-driven construction of the unified model means that bottom-up approach is completed and thus the ultimate goal of top-down approach is defined. This may some clues to formulate the gauge/gravity duality more generally, including quantum corrections in supergravity or string theory.

# A Supplement for deep learning to build our AdS/QCD model

In this appendix we provide details of our deep learning architecture. Our Python code for the machine learning is written on the basis of the code used in Ref. [6]. The latter code is available at github [29] and we revise the forward function and the regularization terms of the code. In addition, the preparation of the input data shown in Fig. 3.3 is necessary. In the following, we provide details about the input layer, the hyperparameters, the loss function and the regularizations, the initial weights, and the dataset generation.

## A.1 Input values at the initial layer

At the end of Sec. 3.1.1, we substitute the initial layer for units $v$, $\pi$ with the asymptotic solution of a typical soft wall model as in (3.14), while the unit $m^2$ receives its value from the input data. We derive (3.14) in the following.

As mentioned, we assume that our model background is asymptotically AdS$_5$. This means that $A(z) \sim -\log z$ and $\Phi(z)$ vanishes at $z \sim 0$. Then the function $B(z)$ defined in (3.7) is approximated by $(2S-1)\log z$. Hence the bulk field equation (3.4) reduces near the AdS boundary $z \sim 0$ to

$$\partial_z\left(\frac{1}{z^{2S-1}}\partial_z v\right) + m^2 \frac{1}{z^{2S-1}} v = 0\,. \tag{A.1}$$

Assuming a power-law configuration $v \sim z^\alpha$, then the equation above reduces to

$$\alpha(\alpha - 2S) z^{\alpha-1-2S} + m^2 z^{\alpha+1-2S} = 0\,, \tag{A.2}$$

which forces us to choose $\alpha = 0, 2S$. We can write a general solution as

$$v = a + bz^{2S}\,. \tag{A.3}$$

According to the AdS/CFT dictionary, the non-normalizable part $a$ corresponds to a source in the boundary theory and the normalizable part $b$ corresponds to the expectation value of an operator associated with the source. Since we are interested in hadron spectra without the source, we set $a = 0$, and moreover we can choose $b = 1$ due to the

[29]The Python code of Ref. [6] is available at `https://github.com/AkinoriTanaka-phys/DL_holographicQCD` and we would like to thank Akinori Tanaka and Akio Tomiya for it.

linearity of equation (A.1). Therefore we estimate the behavior of $v$ near the boundary as

$$v \sim z^{2S} \qquad (z \sim 0) \tag{A.4}$$

which also derives $\pi \sim 2Sz^{2S-1}$, that is (3.14).

## A.2 Hyperparameters

As we described briefly in Sec. 3.1.3, our hyperparameters $N, \Delta z, \epsilon$ in our neural network are fixed by carefully looking at discretization errors. Here we describe how to choose the value of the hyperparameters. We choose $\Delta z$ first, then determine the others. For the evaluation of the discretization errors, we need some analytic solutions for comparison, and we adopt the fluctuation solutions of Ref. [9].

FIg. A.1 shows the lowest solution $v_0(z)$ of the equation of motion of bulk field, which is $v(z)$ with $m = m_{n=0}$ of the model [9]. Both the analytic solution and the numerical solution are plotted. The numerical solution is obtained by Euler method with width $\Delta z = 0.2$. As mentioned in Sec. 3.1.3, we have to look at the location where the solution converges, and also at the difference between the analytic solution and the numerical solution.

First, the plot shows that the analytic $v_0$ almost touches the $z$ axis around $z = 4$. This suggests to set $N = 20$ in order to discriminate the normalizability of solution. Next, the numerical solution approaches 0.2, not 0, due to the discretization error. So we have to choose $\epsilon$ greater than 0.2. From the analysis above, we set these hyperparameters to the values shown in TABLE 3.3.

Of course, we may choose a smaller $\Delta z$ and a larger $N$. However, the discretization error does not change so much, while a larger $N$ makes the computation too heavy because the neural network becomes deeper.

## A.3 Loss function and regularization

The total loss function we use is

$$E' = E + \sum_i p_i \,, \tag{A.5}$$

where $E$ is an L1 loss function, which is commonly used in binary classification. Denoting $\boldsymbol{y}'$ as the output of the neural network and $\boldsymbol{y}$ as the output part of the training

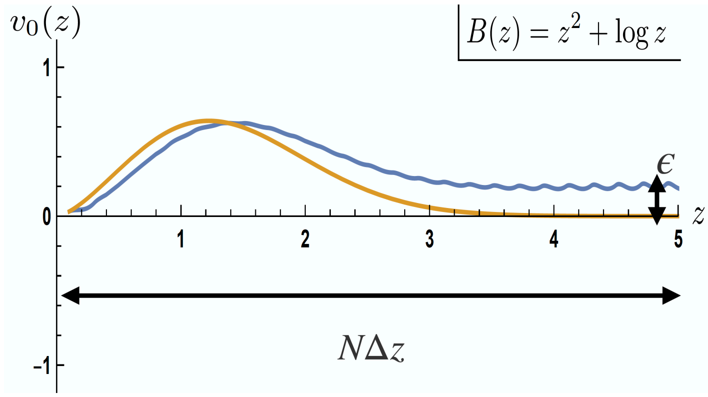


Figure A.1: The ground sate solution of (3.4) with the model background given in Ref. [9] ($B(z) = z^2 + \log z$), solved analytically (yellow line) and numerically (blue line). The blue line interpolates the plots of the numerical solution.

data, then the loss function is made of the L1 distance $\boldsymbol{y}' - \boldsymbol{y}$,

$$E(\boldsymbol{y}' - \boldsymbol{y}) = \frac{1}{d} \sum_{i}^{d} |y'_i - y_i| \,. \tag{A.6}$$

Here $i$ labels the data and $d$ is the number of the data.

The output of our neural network takes a binary value 0 or 1, which is transformed from the unit value of $v$ at the $N$th layer by its normalizability condition. This transformation is given by a smeared box (step) function which was also used in Ref. [6]. For more details, see the function named "t" in the code of Ref. [6].

The loss function (A.5) contains a sum of $p_i$'s, which are the regularizations. Explicitly, they have the following form:

$$\begin{cases} p_1 = \sum_{l=1}^{N} c_{1,l} \left( \frac{2S-1}{l\Delta z} - B'^{(l)} \right)^2 \\ p_2 = \sum_{l=1}^{N} c_{2,l} \left( B'^{(l)} - B'^{(l-1)} \right)^2 \\ p_3 = \sum_{l=1}^{N} c_{3,l} \left( B'^{(l)} - 2B'^{(l-1)} + B'^{(l-2)} \right)^2 \\ p_4 = \sum_{l=1}^{N} c_{4,l} \, \mathrm{relu}\left( B'^{(l-1)} - B'^{(l)} + \delta \right) \end{cases} \tag{A.7}$$

Here $B'^{(l)}$ denotes the weight at $l$-th layer, or equivalently $B'(l\Delta z)$. And the coefficient constant $c_{i,l}$ determines how their constraints are effective as the regularization. There are four kinds of regularizations, $p_i$ ($i = 1, 2, 3, 4$). In the following we explain each in detail.

$p_1$ is the regularization to require that the emergent background is asymptotically AdS. Note that $S$ is spin of meson whose mass spectrum we use as the input, and this factor comes from (3.7). Since this constraint is only for the boundary region of the 5-dimensional geometry, we turn it on only at the first few layers. We set most of $c_{1,l}$ to 0. When we train the network with the $\rho$ meson spectrum, we use the following coefficients:

$$\{c_{1,l}\} = \{0.001, 0.0001, 0.0001, 0, \cdots, 0\} . \tag{A.8}$$

$p_2$ and $p_3$ are the regularizations to require that the emergent background is a smooth geometry. This constraint is necessary to be imposed over all the layers layer but the first few. So, in the $\rho$ meson case, we impose $p_2$ regularization on the 4th layer and deeper layers. For $p_3$, after some tuning, we find that it is enough to impose it from the 7th layer. The coefficients used in the $\rho$ meson training is shown below.

$$\begin{aligned} \{c_{2,l}\} &= \{0, 0, 0, 0.00001, 0.00001, 0.00001, 0.0001, \cdots\} , \\ \{c_{3,l}\} &= \{0, 0, 0, 0, 0, 0, 0.0001, \cdots\} . \end{aligned} \tag{A.9}$$

$p_4$ is the regularization to require that the weight $B'(z)$ is a monotonously increasing function. "relu" is a built-in function of machine learning package, which is defined as

$$\mathrm{relu}(x) = \begin{cases} 0 & \text{for} \quad x \leq 0 \\ x & \text{for} \quad x > 0 \end{cases} \tag{A.10}$$

Hence, if $B'$ decreases along two layers, this regularization provide a positive loss. A small constant $\delta$ plays a roll to require that $B'$ should increase at least by $\delta$. A nonzero small $\delta$ is necessary to train the $a_2$ meson data in our case. The $p_4$ regularization is to require that $B(z)$ should provide the "wall"-like behavior not to have a continuum spectra. For that, we need this $p_4$ regularization at the large $z$ region, otherwise the model allows some unexpected continuous spectrum at a larger mass. The coefficient used in the $\rho$ meson training is the same as that of $p_3$,

$$\{c_{4,l}\} = \{0, 0, 0, 0, 0, 0, 0.01, \cdots\} . \tag{A.11}$$

All the coefficients above is for the $\rho$ meson training. For the $a_2$ meson training, we choose the coefficients as follows:

$$
\begin{aligned}
&c_{1,1} = 0.01\,, \\
&c_{1,i} = 0.001\,(i = 2, \cdots, 8)\,, \\
&c_{3,i} = 0.01\,(i = 9, \cdots, 12)\,, \\
&c_{3,j} = 0.005\,(j = 13, \cdots, 21)\,, \\
&c_{3,k} = 0.001\,(k = 22, \cdots, 80)\,, \\
&c_{4,i} = 10\,(i = 61, \cdots, 80)\,,
\end{aligned}
\tag{A.12}
$$

and the other components are put to zero.

## A.4 Initial weight

For a successful training, we need to control the initial values of the weights to some extent. In the $\rho$ meson training, we initially sample the values of the weights at the $l$-th layer from the normal distribution whose mean is $1 + 0.5l$ with the standard deviation $0.3l$ when we initialize the neural network. In the $a_2$ meson training, we initially sample them from the normal distribution whose mean is $3/(0.5l + 0.05) + 0.05l - 7$ with the standard deviation 10.

## A.5 Training dataset

Here we present our Python code to generate the dataset given in Fig. 3(b) and Fig. 3(c). Our training trials observe that the success of the training depends on the range of the positive data values and also the local density of data points, which is presented explicitly in the following codes for the $\rho$ meson and for the $a_2$ meson.

## A.6 Metrics trained by neural ODE

In this appendix, we describe the regularization methods and the training methods of our neural ODE in more details. The numerical data of the trained function $h$ is described in Table 5.2 with the definition (5.5).

In Fig. A.2, we show our numerical results of the neural ODE. As the figure shows, the fit functions $h(\eta)$ reproduces the lattice QCD data well.

Let us describe our regularization method of the neural ODE. As mentioned in [41], the merit of the neural ODE is that there is no need of the smoothing regularization which was employed in the original AdS/DL research [5, 6] to regard deep neural networks to be spacetimes. However, still we need some regularization to make sure that

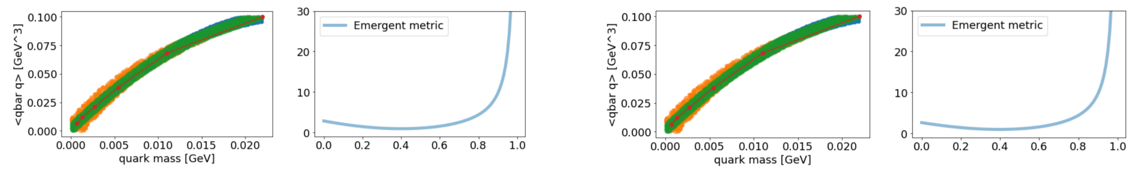


Figure A.2: The training results of the neural ODE. (a) and (b) are for our successful trial #1 and #2, respectively. In each figure, the left panel shows how the QCD lattice data (shown green) is successfully reproduced by the model (orange + green). Red lines are the original central points of the lattice QCD data. The right panel in each figure shows the trained metric function $h(\tilde{\eta})$ where $\tilde{\eta} \equiv 1 - \eta$ (the region for the training is $0 \leq \eta \leq 1$ in the unit $L = 1$). At $\tilde{\eta} = 1$, the black hole horizon exists, while $\tilde{\eta} = 0$ is supposed to be the AdS asymptotic region, thus approaches to $h = 4$.

the asymptotic region of the function $h$ should approach the constant $h = 4$ so that the spacetime is asymptotically $\mathrm{AdS}_5$. Furthermore, since we employ Einstein-dilaton system for the holographic QCD, the emergent metric needs to approach $h = 4$ in a specific manner. When the asymptotic behavior is approximated by $h(\eta) \simeq 4 - 4B_h \exp[-p\,\eta]$, the Einstein-dilaton system requires $4 < p \leq 8$ (see (5.44)).

To satisfy these two kinds of the requirement, we put the following regularization terms in the loss function $\mathcal{L}$ of the neural ODE:

$$\mathcal{L}_h \equiv c_1 (h(1) - 4)^2 + c_2 \left( \frac{h'(1)}{h(1) - 4} + 4 \right)^2 \tag{A.13}$$

where $c_1$ and $c_2$ are some positive numbers called regularization coefficients which are hyperparameters of the machine learning. The first term brings the trained metric function at $\eta = 1$ closer to the AdS value $h = 4$, and the second term brings the exponent $p$ closer to the value $p = 4$ which is the central value of the allowed region for $p$ in the Einstein-dilaton system.

During the training, we have to tune the initial conditions and the magnitude of the regularization for the training to be successful. The training architecture other than the regularizations is identical to that employed in [41]. Our successful training is obtained by the following procedure. First, we choose the initial conditions as follows:

$$\begin{aligned} &L = 1.0, \quad \lambda = 0.3, \\ &b_1 = -4.10, \quad b_3 = 7.00, \quad b_5 = 0.00\,. \end{aligned} \tag{A.14}$$

These values for $b_1$, $b_3$ and $b_5$ are suggested from the functional form of $h$ of the training results given in [41, 6]. We choose $c_1 = 0.01$ and $c_2 = 0.0000027$ (we tune the maximum value of $c_2$ for the training to be successful). Then after 10000 epochs of the training, we reach

$$
\begin{aligned}
&L = 3.349, \quad \lambda = 0.008769, \\
&b_1 = -3.819, \quad b_3 = 6.657, \quad b_5 = -0.4160\,.
\end{aligned}
\tag{A.15}
$$

We use this data as another initial condition for the training with $c_1 = 0.01$ and $c_2 = 0.001$, and after 30000 epochs, we obtain the training result #1 given in Table 5.2. Finally, using the result #1 as an initial condition, we make a training with $c_1 = 0.01$ and $c_2 = 0.003$ for 10000 epochs to find the training result #2 given in Table 5.2.

In summary, the difference between the results #1 and #2 is the strength of the second term in the regularization (A.13). The training result #2 has a value of $B_h$ closer to $p = 4$, while both of #1 and #2 have the values of $p$ in the consistency range $4 < p \leq 8$.

As for the training, we also note here that we checked if the resulting $\Phi(\eta)$ is monotonically decreasing function, as already declared in Eq.(5.8). Or equivalently,

$$
v(\eta) > h(\eta) \quad \text{for} \quad \forall\eta,
\tag{A.16}
$$

otherwise, $V_D(\Phi)$ turns out to be a multi-valued function unless something miraculous happens. With a given trained metric $h(\eta)$, Inequality(A.16) is the second obstacle after Inequality(5.44) that the trained $h(\eta)$ has to overcome. In fact, before the modifications described in Sec.5.1, many trained data for $h(\eta)$ with poor initial conditions, or a rough calculation accuracy caused multi-valued dilaton potential and were rejected.

# References


[1] J.M. Maldacena, *The Large N limit of superconformal field theories and supergravity*, *Adv. Theor. Math. Phys.* **2** (1998) 231 [hep-th/9711200].

[2] G.E. Hinton and R. Salakhutdinov, *Reducing the dimensionality of data with neural networks*, *Science* **313** (2006) 504 .

[3] Y. LeCun, Y. Bengio and G. Hinton, *Deep learning*, *Nature* **521** (2015) 436.

[4] Y. Bengio and Y. LeCun, *Scaling learning algorithms towards AI*, 2007.

[5] K. Hashimoto, S. Sugishita, A. Tanaka and A. Tomiya, *Deep learning and the AdS/CFT correspondence*, *Phys. Rev. D* **98** (2018) 046019 [1802.08313].

[6] K. Hashimoto, S. Sugishita, A. Tanaka and A. Tomiya, *Deep Learning and Holographic QCD*, *Phys. Rev. D* **98** (2018) 106014 [1809.10536].

[7] J. Erlich, E. Katz, D.T. Son and M.A. Stephanov, *QCD and a holographic model of hadrons*, *Phys. Rev. Lett.* **95** (2005) 261602 [hep-ph/0501128].

[8] L. Da Rold and A. Pomarol, *Chiral symmetry breaking from five dimensional spaces*, *Nucl. Phys. B* **721** (2005) 79 [hep-ph/0501218].

[9] A. Karch, E. Katz, D.T. Son and M.A. Stephanov, *Linear confinement and AdS/QCD*, *Phys. Rev. D* **74** (2006) 015005 [hep-ph/0602229].

[10] K. Hashimoto, *AdS/CFT correspondence as a deep Boltzmann machine*, *Phys. Rev. D* **99** (2019) 106017 [1903.04951].

[11] Y.-Z. You, Z. Yang and X.-L. Qi, *Machine Learning Spatial Geometry from Entanglement Features*, *Phys. Rev. B* **97** (2018) 045153 [1709.01223].

[12] W.-C. Gan and F.-W. Shu, *Holography as deep learning*, *Int. J. Mod. Phys. D* **26** (2017) 1743020 [1705.05750].

[13] J.-W. Lee, *Quantum fields as deep learning*, *J. Korean Phys. Soc.* **76** (2020) 684 [1708.07408].

[14] H.D.I. Abarbanel, P.J. Rozdeba and S. Shirman, *Machine learning: Deepest learning as statistical data assimilation problems*, *Neural Computation* **30** (2017) 2025.

[15] T. Akutagawa, K. Hashimoto and T. Sumimoto, *Deep Learning and AdS/QCD*, *Phys. Rev. D* **102** (2020) 026020 [2005.02636].

[16] K. Hashimoto, K. Ohashi and T. Sumimoto, *Deriving the dilaton potential in improved holographic QCD from the meson spectrum*, *Phys. Rev. D* **105** (2022) 106008 [2108.08091].

[17] K. Hashimoto, K. Ohashi and T. Sumimoto, *Deriving dilaton potential in improved holographic QCD from chiral condensate*, 2209.04638.

[18] S.S. Gubser, I.R. Klebanov and A.M. Polyakov, *Gauge theory correlators from noncritical string theory*, *Phys. Lett. B* **428** (1998) 105 [hep-th/9802109].

[19] E. Witten, *Anti-de Sitter space and holography*, *Adv. Theor. Math. Phys.* **2** (1998) 253 [hep-th/9802150].

[20] A. Karch and E. Katz, *Adding flavor to AdS / CFT*, *JHEP* **06** (2002) 043 [hep-th/0205236].

[21] T. Sakai and S. Sugimoto, *Low energy hadron physics in holographic QCD*, *Prog. Theor. Phys.* **113** (2005) 843 [hep-th/0412141].

[22] S. Hong, S. Yoon and M.J. Strassler, *Adjoint trapping: A New phenomenon at strong 't Hooft coupling*, *JHEP* **03** (2006) 012 [hep-th/0410080].

[23] S. Hong, S. Yoon and M.J. Strassler, *On the couplings of vector mesons in AdS / QCD*, *JHEP* **04** (2006) 003 [hep-th/0409118].

[24] Particle Data Group collaboration, *Review of Particle Physics*, *Phys. Rev. D* **98** (2018) 030001.

[25] G. Carleo, I. Cirac, K. Cranmer, L. Daudet, M. Schuld, N. Tishby et al., *Machine learning and the physical sciences*, *Rev. Mod. Phys.* **91** (2019) 045002 [1903.10563].

[26] U. Gursoy and E. Kiritsis, *Exploring improved holographic theories for QCD: Part I*, *JHEP* **02** (2008) 032 [0707.1324].

[27] U. Gursoy, E. Kiritsis and F. Nitti, *Exploring improved holographic theories for QCD: Part II*, *JHEP* **02** (2008) 019 [0707.1349].

[28] E. Katz, A. Lewandowski and M.D. Schwartz, *Tensor mesons in AdS/QCD*, *Phys. Rev. D* **74** (2006) 086004 [hep-ph/0510388].

[29] S.S. Gubser and A. Nellore, *Mimicking the QCD equation of state with a dual black hole*, *Phys. Rev. D* **78** (2008) 086007 [0804.0434].

[30] P. Breitenlohner and D.Z. Freedman, *Positive Energy in anti-De Sitter Backgrounds and Gauged Extended Supergravity*, *Phys. Lett. B* **115** (1982) 197.

[31] P. Breitenlohner and D.Z. Freedman, *Stability in Gauged Extended Supergravity*, *Annals Phys.* **144** (1982) 249.

[32] J.M. Maldacena, *Wilson loops in large N field theories*, *Phys. Rev. Lett.* **80** (1998) 4859 [hep-th/9803002].

[33] S.-J. Rey and J.-T. Yee, *Macroscopic strings as heavy quarks in large N gauge theory and anti-de Sitter supergravity*, *Eur. Phys. J. C* **22** (2001) 379 [hep-th/9803001].

[34] Y. Kinar, E. Schreiber and J. Sonnenschein, *Q anti-Q potential from strings in curved space-time: Classical results*, *Nucl. Phys. B* **566** (2000) 103 [hep-th/9811192].

[35] M. Luscher, *Symmetry Breaking Aspects of the Roughening Transition in Gauge Theories*, *Nucl. Phys. B* **180** (1981) 317.

[36] G.S. Bali and K. Schilling, *Running coupling and the Lambda parameter from SU(3) lattice simulations*, *Phys. Rev. D* **47** (1993) 661 [hep-lat/9208028].

[37] O. Andreev and V.I. Zakharov, *Heavy-quark potentials and AdS/QCD*, *Phys. Rev. D* **74** (2006) 025023 [hep-ph/0604204].

[38] C.D. White, *The Cornell potential from general geometries in AdS / QCD*, *Phys. Lett. B* **652** (2007) 79 [hep-ph/0701157].

[39] Y. Kinar, E. Schreiber, J. Sonnenschein and N. Weiss, *Quantum fluctuations of Wilson loops from string models*, *Nucl. Phys. B* **583** (2000) 76 [hep-th/9911123].

[40] T.Q. Chen, Y. Rubanova, J. Bettencourt and D.K. Duvenaud, *Neural ordinary differential equations*, in *Neural Information Processing Systems*, 2018.

[41] K. Hashimoto, H.-Y. Hu and Y.-Z. You, *Neural ordinary differential equation and holographic quantum chromodynamics*, *Mach. Learn. Sci. Tech.* **2** (2021) 035011 [2006.00712].

[42] W. Unger, *The chiral phase transition of QCD with 2+1 flavors : a lattice study on Goldstone modes and universal scaling*, 2010.

[43] P. Petreczky, *Quarkonium in Hot Medium*, *J. Phys. G* **37** (2010) 094009 [1001.5284].

[44] F. Ruehle, *Data science applications to string theory*, *Phys. Rept.* **839** (2020) 1.

[45] R. Vasseur, A.C. Potter, Y.-Z. You and A.W.W. Ludwig, *Entanglement Transitions from Holographic Random Tensor Networks*, *Phys. Rev. B* **100** (2019) 134203 [1807.07082].

[46] H.-Y. Hu, S.-H. Li, L. Wang and Y.-Z. You, *Machine Learning Holographic Mapping by Neural Network Renormalization Group*, *Phys. Rev. Res.* **2** (2020) 023369 [1903.00804].

[47] J. Tan and C.-B. Chen, *Deep learning the holographic black hole with charge*, *Int. J. Mod. Phys. D* **28** (2019) 1950153 [1908.01470].

[48] D. Krefl and R.-K. Seong, *Machine Learning of Calabi-Yau Volumes*, *Phys. Rev. D* **96** (2017) 066014 [1706.03346].

[49] Y.-H. He, *Deep-Learning the Landscape*, 1706.02714.

[50] F. Ruehle, *Evolving neural networks with genetic algorithms to study the String Landscape*, *JHEP* **08** (2017) 038 [1706.07024].

[51] J. Carifio, J. Halverson, D. Krioukov and B.D. Nelson, *Machine Learning in the String Landscape*, *JHEP* **09** (2017) 157 [1707.00655].

[52] K. Hashimoto, *Building bulk from Wilson loops*, *PTEP* **2021** (2021) 023B04 [2008.10883].

[53] Y.-K. Yan, S.-F. Wu, X.-H. Ge and Y. Tian, *Deep learning black hole metrics from shear viscosity*, *Phys. Rev. D* **102** (2020) 101902 [2004.12112].

[54] M. Song, M.S.H. Oh, Y. Ahn and K.-Y. Kima, *AdS/Deep-Learning made easy: simple examples*, *Chin. Phys. C* **45** (2021) 073111 [2011.13726].